

High-Speed Atomic Force Microscopy

Toshio Ando and Takayuki Uchihashi

Abstract Biological macromolecules are responsible for the vital activities of life. Among the various approaches to understanding their functional mechanisms, the most straightforward approach is to directly visualize the structure and dynamic action of biological macromolecules at high spatial and temporal resolution. However, the microscopy needed to enable such visualization was not available until the recent development of high-speed atomic force microscopy (AFM). This allows the recording of images of biological samples at 30–60 ms/frame without disturbing delicate biomolecular interactions and hence the delineation of time-series events that occur in biomolecules at work. This chapter describes various devices and techniques developed for high-speed AFM and imaging studies performed on several protein systems.

17.1. Introduction

The dynamic aspect of biological macromolecules is one of the essential attributes. Their functions are produced through their dynamic structural changes and dynamic interactions with other molecules. Furthermore, their functions are produced at the single-molecule level. Therefore, it is important to observe their dynamic behaviors straightforwardly at the single-molecule level to understand their functional mechanisms. As seen in other chapters in this book, single-molecule fluorescence microscopy has been widely exploited for this type of observation. It enables the measurement of translational or rotational motions of individual fluorophores attached to biological molecules and in some cases the measurement of association and dissociation reactions between biological molecules. However, it requires bridging the gap between the recorded fluorescence images and the actual behavior of the labeled biological molecules.

The atomic force microscope (AFM) is capable of directly visualizing unstained biological samples in liquids at nanometer resolution. However, unlike fluorescence microscopy, its imaging rate is low, and hence it cannot trace the fast dynamic processes within the sample. The low imaging rate mainly arises from the fact that AFM uses mechanical sensing and mechanical scanning to detect the sample height at each pixel. Another weak point of

T. Ando and T. Uchihashi • Department of Physics, Kanazawa University, Kakuma-machi, Kanazawa 920-1192 Japan, and CREST, JST, Sanban-cho, Chiyoda-ku, Tokyo 102-0075, Japan

AFM also results from the mechanical sensing: The mechanical tip–sample interaction tends to disturb delicate samples and, in the worst-case situation, disrupts fragile samples. In the last decade, various efforts have been made to increase the scan speed, although little attention has been paid to reconciling the fast imaging capability with low-invasiveness imaging. Recent efforts toward this reconciliation have given rise to high-speed AFM, which enables the observation of dynamic biomolecular processes at an imaging rate of 30–60 ms/frame without significantly disturbing delicate biomolecular interactions.

Because this new microscopy has appeared only recently, the user population and the number of successful imaging studies are still limited. We hope that this situation will change in a few years in line with the increase in the availability of commercial high-speed AFM. In this chapter, we first describe the imaging rate as a function of various parameters and also discuss key devices and techniques for high-speed imaging. Next, we give some examples of the successful imaging of dynamic biomolecular processes and describe some techniques and problems associated with the imaging. For the history of high-speed AFM development and the future prospects of high-speed AFM studies in biological research, see recent review articles (e.g., Ando et al., 2007; 2008a, b).

17.2. Basic Principle of AFM and Various Imaging Modes

A typical AFM setup is depicted in Figure 17.1. The sample surface is touched with a sharp tip attached to the free end of a soft cantilever while the sample stage is scanned horizontally (x and y directions). On touching the sample, the cantilever is deflected. Among several methods of sensing this deflection, optical beam deflection (OBD) sensing is often used because of its simplicity; a collimated laser beam is focused onto the cantilever and reflected back into closely spaced photodiodes (a position-sensitive photodetector [PSPD]) whose photocurrents are fed into a differential amplifier. The output of the differential amplifier is proportional to the cantilever deflection. During the raster scan of the sample stage, the detected deflection is compared with the target value (set-point deflection), and then the stage is moved in the z direction to minimize the error signal (the difference between the detected and set-point deflections). This closed-loop feedback operation can maintain the cantilever deflection (hence, the tip–sample interaction force) at the set-point value. The resulting three-dimensional (3D) movement of the sample stage approximately traces the sample surface, and hence a topographic image can be constructed, by using a computer, from the electric signals that are used to drive the sample stage scanner in the z direction. In the operation mode just described (constant-force mode; one of the direct current [DC] modes or contact modes), the cantilever tip, which is always in contact with the sample, exerts relatively large lateral forces on the sample because the spring constant of the cantilever is large in the lateral direction.

To avoid the foregoing problem, tapping-mode AFM (one of the dynamic modes) was invented (Zhong et al., 1993), in which the cantilever is oscillated in the z direction at (or near) its resonant frequency. In this mode, the tip intermittently taps the sample surface at the end of bottom swings. Therefore, little lateral tip force is exerted on the sample, provided that the velocity of the sample stage lateral movement is not too high compared with that of cantilever movement in the z direction. The cantilever oscillation amplitude is reduced by the repulsive interaction between the tip and the sample. Therefore, this mode is also called the amplitude modulation (AM) mode. The amplitude signal is usually generated by a root mean square (RMS)-to-DC converter and is maintained at a constant level (set-point amplitude) by a feedback operation. In AM-AFM, the cantilever oscillation amplitude decreases not only

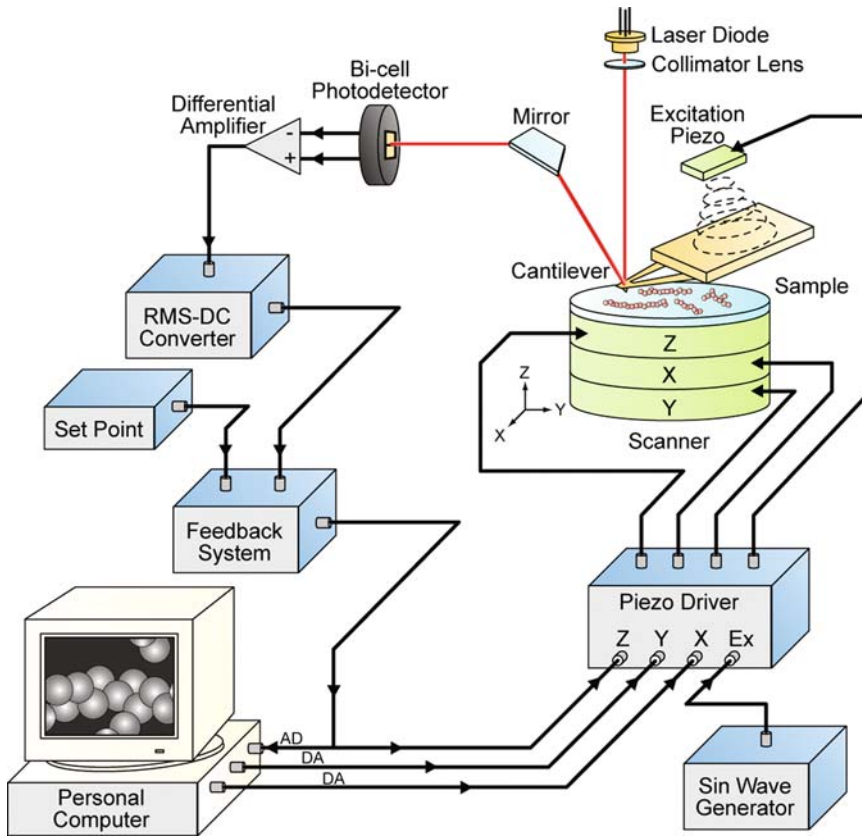


Figure 17.1. Schematic presentation of the tapping-mode AFM system. In the constant-force mode, the excitation piezoelectric actuator and the root mean square-to-direct current (RMS-to-DC) converter are omitted.

by energy dissipation due to the tip-sample interaction, but also by a shift in the cantilever resonant frequency caused by the interaction (Tamayo and García, 1996; Bar et al., 1997; Cleveland et al., 1998). The repulsive interaction produces a positive shift in the resonant frequency because the apparent spring constant k_c of the cantilever is changed by the gradient of the interaction force ($k \equiv \partial f / \partial z$; k is negative for the repulsive interaction). As the excitation frequency is fixed at (or near) the resonant frequency, this frequency shift produces a phase shift of the cantilever oscillation relative to the excitation signal. When this phase shift is maintained by a feedback operation and an image is constructed from the electric signals used for driving the z -scanner, the imaging mode is called the phase modulation (PM) mode. Alternatively, one can construct a phase-contrast image from the phase signal while maintaining the amplitude at a constant level by a feedback operation. More details of the PM mode and phase-contrast imaging are given in Sections 17.4.7 and 17.5.5. Instead of using a fixed frequency, it is possible to set the excitation frequency automatically to the varying resonant frequency of the cantilever by using a self-oscillation circuit (Albrecht et al., 1991; Giessibl, 1995). In this case, the phase of the cantilever oscillation relative to the excitation signal is always maintained at -90° , and the resonant frequency shift is maintained at a constant level by feedback operation. This mode is called the frequency modulation (FM) mode.

17.3. Imaging Rate and Feedback Bandwidth

AFM users do not seem to well understand how a high imaging rate is possible with a given AFM instrument. In this section, on the basis of an idea previously presented (Kodera et al., 2006), we derive the quantitative relationship between the feedback bandwidth and the various factors involved in AFM devices and the scanning conditions in the tapping mode.

17.3.1. Image Acquisition Time and Feedback Bandwidth

Instrumental factors that determine the maximum possible imaging rate are the feedback bandwidth and the maximum frequency at which the scanner can operate without producing unwanted vibrations. As the latter factor is obvious, we only describe the feedback bandwidth. Supposing that a frame is acquired in time T over the scan range $W \times W$ with N scan lines, then the scan velocity V_s in the x direction is given by $V_s = 2WN/T$. Assuming that the sample has a sinusoidal shape with periodicity λ , we see that the scan velocity V_s requires feedback operation at frequency $f = V_s/\lambda$ to maintain the tip-sample distance. The feedback bandwidth f_B should be greater than or equal to f and can therefore be expressed as

$$f_B \geq 2WN/\lambda T \quad (17.1)$$

Equation (17.1) gives the relationship between the frame acquisition time T and the feedback bandwidth f_B . For example, for $T = 30$ ms with $W = 240$ nm and $N = 100$, the scan velocity is 1.6 mm/s. When λ is 10 nm, $f_B \geq 160$ kHz is required to attain this scan velocity. Note that the maximum scan velocity achievable under a given feedback bandwidth depends on the spatial frequency contained in the sample topography, and therefore it is not an appropriate index for evaluating the instrument speed performance.

17.3.2. Feedback Bandwidth as a Function of Various Factors

Various devices are contained in the feedback loop (closed loop) (see Figure 17.1). The sum of the time delays ($\Delta\tau$) that occur with these devices is called “open-loop time delay.” Note that the time delay (or phase delay θ) of the closed-loop feedback control is different from the open-loop time delay (or phase delay φ). There is the relationship $\theta \sim 2\varphi$ when the feedback gain is maintained at ~ 1 (Ando et al., 2008b). Thus, $\theta \sim 2\pi f(2\Delta\tau) = 4\pi f\Delta\tau$, where f is the feedback frequency. In tapping-mode AFM, the main delays are the time (τ_a) required to measure the cantilever oscillation amplitude, the cantilever response time (τ_c), the z -scanner response time (τ_s), the integral time (τ_I) of error signals in the feedback controller, and the parachuting time (τ_p). Here, “parachuting” means that the cantilever tip completely detaches from the sample surface at a steeply inclined region of the sample and cannot quickly land on the surface again. The minimum τ_a is given by $1/(2f_c)$, where f_c is the cantilever’s fundamental resonant frequency. Cantilevers and the z -scanner are second-order resonant systems. Therefore, τ_c and τ_s are expressed by $Q_c/(\pi f_c)$ and $Q_s/(\pi f_s)$, respectively, where f_s is the resonant frequency of the z -scanner and Q_c and Q_s are, respectively, the quality factors of the cantilever and the z -scanner. The τ_I and τ_p are functions of various parameters, the approximate analytical expressions of which will be given later. The feedback bandwidth f_B is usually defined by the feedback frequency that results in a phase delay of $\pi/4$. On the basis of this definition, f_B is approximately expressed as

$$f_B = \alpha \frac{f_c}{8} / \left(1 + \frac{2Q_c}{\pi} + \frac{2Q_s f_c}{\pi f_s} + 2f_c (\tau_p + \tau_I + \delta) \right) \quad (17.2)$$

where δ represents the sum of other time delays and α represents a factor related to the phase compensation effect given by the D component in the proportional integral derivative (PID) feedback controller or in an additional phase compensator. According to our experience, $\alpha \sim 2.8$. Thus, from Eqs. (17.1) and (17.2), we can estimate the maximum possible imaging rate in a given tapping-mode AFM setup by examining the open-loop time delay $\Delta\tau$. However, this estimation must be modified depending on the sample to be imaged because the allowable maximum phase delay depends on the strength or fragility of the sample. In the next section, we determine the allowable maximum phase delay.

17.3.3. Feedback Operation and Parachuting

To maintain the amplitude of an oscillating cantilever at a constant level while the sample stage is being raster-scanned in the xy directions, the detected amplitude is compared with the set-point amplitude. Their difference (error signal) is fed to a PID feedback controller. The PID output is fed to a voltage amplifier to drive the z -piezoactuator. This is repeated until the error signal is minimized. To reduce the tapping force exerted from the oscillating tip to the sample, the set-point amplitude should be set close to the cantilever's free oscillation amplitude. However, under this condition, the tip tends to detach completely from the sample surface, particularly at a steep downhill region of the sample. Once detached, the error signal is constant (i.e., saturated at a small level) irrespective of how far the tip is separated from the sample surface. The gain parameters of the PID controller can be increased to reduce the parachuting time. However, such large gains in turn produce an overshoot in the uphill region of the sample, which promotes parachuting around the top region of the sample and leads to instability in the feedback operation.

As has been seen, parachuting is problematic, particularly for high-speed bioAFM in which the tapping force must be minimized. During parachuting, the information of sample topography is completely lost. Here, we determine the conditions that cause parachuting, and obtain a rough estimate of the parachuting time and its effect on the feedback bandwidth (Kodera et al., 2006). The theoretical results obtained here are compared with experimental data to refine the analytical expression for the parachuting time.

When a sample having a sinusoidal shape with periodicity λ and maximum height h_0 is scanned at velocity V_s in the x direction, the sample height $S(t)$ under the cantilever tip varies as

$$S(t) = \frac{h_0}{2} \sin(2\pi ft) \quad (17.3)$$

where $f = V_s/\lambda$. When no parachuting occurs, the z -scanner moves as

$$Z(t) = -\frac{h_0}{2} \sin(2\pi ft - \theta) \quad (17.4)$$

The feedback error ("residual topography" ΔS) is thus expressed as

$$\Delta S(t) = S(t) + Z(t) = h_0 \sin \frac{\theta}{2} \cos \left(2\pi ft - \frac{\theta}{2} \right) \quad (17.5)$$

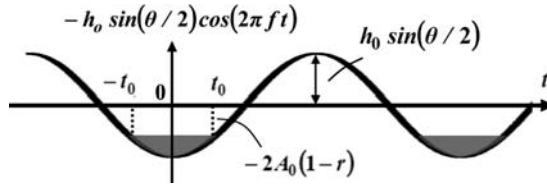


Figure 17.2. The residual topography to be sensed by a cantilever tip under feedback control. When the maximum height of the residual topography is greater than the difference $2A_0(1-r)$, the tip completely detaches from the surface at an area around the bottom. The untouched areas are shown in gray. The average tip-surface separation $\langle d \rangle$ at the end of the cantilever's bottom swing is given by $\langle d \rangle = \frac{1}{2t_0} \int_{-t_0}^{t_0} [-2A_0(1-r) + h_0 \sin(\theta/2) \cos(2\pi ft)] dt$, where $t_0 = \beta/2\pi f$ (see text). This integral results in $\langle d \rangle = 2A_0(1-r)(\tan \beta/\beta - 1)$.

The cantilever tip feels this residual topography (Figure 17.2) in addition to a constant height of $2A_0(1-r)$, where A_0 is the free oscillation amplitude of the cantilever and r is the dimensionless peak-to-peak amplitude set-point. When the set-point peak-to-peak amplitude is denoted as A_s , we have $r = A_s/(2A_0)$.

Because of feedback error, an extra force is exerted onto the sample, the maximum value of which corresponds to a distance of $h_0 \sin(\theta/2)$. Therefore, an allowable maximum phase delay θ_a , which depends on the sample strength, is determined by this distance. The amplitude set-point r is usually determined by compromising between two factors: (1) decrease in tapping force with increasing r , and (2) decrease in the feedback bandwidth with increasing r owing to parachuting. Therefore, the allowable maximum extra force approximately corresponds to $\sim 2A_0(1-r)$, which gives the relationship $\sin(\theta_a/2) \sim (2A_0/h_0)(1-r)$.

When $\Delta S(t) + 2A_0(1-r) > 0$, no parachuting occurs. Therefore, the maximum set-point r_{\max} for which parachuting does not occur is given by

$$r_{\max} = 1 - \frac{h_0}{2A_0} \sin \frac{\theta}{2} \quad (17.6)$$

Equation (17.6) indicates that r_{\max} decreases with increasing $h_0/2A_0$ and with increasing phase delay in the feedback operation.

The parachuting time is a function of various parameters, such as the sample height h_0 , the free oscillation amplitude A_0 of the cantilever, the set-point r , the phase delay θ , and the cantilever resonant frequency f_c . Its analytical expression cannot be obtained exactly. As a first approximation, we assume that during parachuting, Eq. (17.5) holds and the z position of the sample stage does not move. During parachuting, the average separation between the sample surface and the tip at the end of the bottom swing is given by $2A_0(1-r)(\tan \beta/\beta - 1)$ (see Figure 17.3), where β is given by

$$\beta = \cos^{-1}\{2A_0(1-r)/[h_0 \sin(\theta/2)]\} \quad (17.7)$$

The feedback gain is usually set to a level at which the separation distance of $2A_0(1-r)$ decreases to approximately zero in a single period of the cantilever oscillation. Therefore, the parachuting time τ_p is expressed as

$$\tau_p = (\tan \beta/\beta - 1)/f_c \quad (17.8)$$

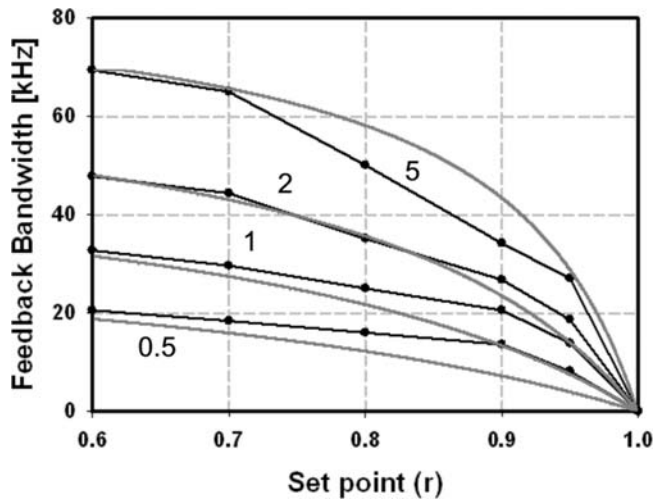


Figure 17.3. Feedback bandwidth as a function of the set-point r and the ratio $2A_0/h_0$ of the free oscillation peak-to-peak amplitude to the sample height. The number attached to each curve indicates the ratio $2A_0/h_0$. The feedback bandwidths were obtained under the following conditions: cantilever resonant frequency, 1.2 MHz; Q factor of cantilever oscillation, 3; resonant frequency of z -scanner, 150 kHz; Q factor of z -scanner, 0.5. The black lines are the experimentally obtained feedback bandwidths using a mock atomic force microscope; the gray lines are the theoretically derived feedback bandwidths.

However, the assumptions under which the average separation during parachuting was derived are different from the reality. As mentioned later (Section 17.3.4), the analytical expression for τ_p should be modified in light of the experimentally obtained feedback bandwidth as a function of r and h_0/A_0 .

The main component of PID control is the integral operation. It is difficult to theoretically estimate the integral time constant τ_I with which the optimum feedback control is attained. Intuitively, τ_I should be longer when a greater phase delay exists in the feedback loop. In other words, when a long phase delay exists, the gain parameters of the PID controller cannot be increased. Therefore, τ_I must be proportional to the height of residual topography relative to the free oscillation amplitude of the cantilever. Because the error signals fed into the PID controller are renewed every (half) cycle of the cantilever oscillation, τ_I must be inversely proportional to the resonant frequency of the cantilever. The feedback gain should be independent of parachuting because the gain is maximized so that optimum feedback control is performed for a nonparachuting regime. Thus, τ_I is approximately expressed as $\tau_I = \kappa h_0 \sin(\theta/2)/(A_0 f_c)$, where κ is a proportion coefficient.

17.3.4. Refinement of Analytical Expressions for τ_p and τ_I

We experimentally measured the feedback bandwidth as a function of $2A_0/h_0$ and r using a mock AFM system containing a mock cantilever and z -scanner (Kodera et al., 2006) (Figure 17.3). The mock cantilever and z -scanner are second-order low-pass filters whose resonant frequencies and quality factors are adjusted to have the corresponding values of a real cantilever and z -scanner. The experimentally obtained feedback bandwidths are shown by the black lines in Figure 17.3. Feedback bandwidths are theoretically calculated using

Eq. (17.2) with κ and β as variables and known values of the other parameters. From this analysis, we obtained the following refined expressions for β and τ_I :

$$\beta = \cos^{-1}\{A_0(1-r)/[5h_0 \sin(\theta/2)]\} \quad (17.9)$$

$$\tau_I = 4h_0 \sin(\theta/2)/(A_0 f_c) \quad (17.10)$$

Feedback bandwidths calculated using these refined expressions are shown by the gray lines in Figure 17.3. They approximately coincide with the experimental data.

17.4. Devices for High-Speed AFM

17.4.1. Small Cantilevers and Related Devices

The cantilever resonant frequency affects the feedback bandwidth via two terms: the amplitude detection time and the cantilever response time [see Eq. (17.2)]. Therefore, cantilevers are the most important devices in high-speed AFM. The resonant frequency f_c and the spring constant k_c of a rectangular cantilever with thickness d , width w , and length L are expressed as

$$f_c = 0.56 \frac{d}{L^2} \sqrt{\frac{E}{12\rho}} \quad (17.11)$$

and

$$k_c = \frac{wd^3}{4L^3} E \quad (17.12)$$

where E and ρ are Young's modulus and the density of the material used, respectively. Young's modulus and the density of silicon nitride (Si_3N_4), which is often used as a material for soft cantilevers, are $E = 1.46 \times 10^{11}$ N/m² and $\rho = 3,087$ kg/m³, respectively. To attain a high resonant frequency and a small spring constant simultaneously, cantilevers with small dimensions must be fabricated.

The small cantilevers recently developed by Olympus are made of silicon nitride and are coated with gold of ~ 20 nm thickness. They have a length of 6–7 μm , a width of 2 μm , and a thickness of ~ 90 nm, which result in resonant frequencies of ~ 3.5 MHz in air and ~ 1.2 MHz in water, a spring constant of ~ 0.2 N/m, and $Q \sim 2.5$ in water. These values in water give the minimum $\tau_a = 0.42$ μs and $\tau_c = 0.66$ μs . We are currently using this type of cantilever, although it is not yet commercially available.

The tip apex radius of the small cantilevers developed by Olympus is ~ 17 nm (Kitazawa et al., 2003), which is too large for the high-resolution imaging of biological samples. We usually use electron-beam deposition (EBD) to form a sharp tip extending from the original tip. A piece of phenol crystal (sublimate) is placed in a small container, the top of which is perforated with holes ~ 0.1 mm in diameter. The container is placed in a scanning electron microscope (SEM) chamber, and cantilevers are placed immediately above the container's holes. Spot-mode electron beam irradiation onto the cantilever tip produces a needle on the original tip at a growth rate of ~ 50 nm/sec. The newly formed tip has an apex radius of

~ 25 nm and is sharpened by plasma etching in argon or oxygen gas, which decreases the apex radius to ~ 4 nm.

We developed an OBD detector for small cantilevers (Ando et al., 2001) (Figure 17.4); a laser beam reflected back from the rear side of a cantilever is collected and collimated using the same objective lens as that used for focusing the incident laser beam onto the cantilever. The focused spot is $3\text{--}4\ \mu\text{m}$ in diameter. The incident and reflected laser beams are separated using a quarter-wavelength plate and a polarization splitter. Our recent high-speed AFM is integrated with a laboratory-made inverted optical microscope with robust mechanics. The focusing objective lens is also used to view the cantilever and the focused laser spot with the optical microscope. The laser driver is equipped with a radio-frequency (RF) power modulator to reduce noise originating in the optics (Fukuma et al., 2005). The photosensor consists of a four-segment Si PIN photodiode (3 pF, 40 MHz) and a custom-made fast amplifier/signal conditioner (~ 20 MHz).

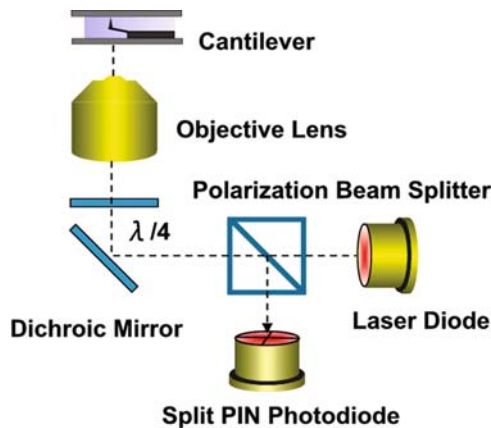


Figure 17.4. Schematic drawing of the objective-lens-type optical beam deflection detection system. The collimated laser beam is reflected up by the dichroic mirror and is incident on the objective lens. The beam reflected at the cantilever is collimated by the objective lens, separated from the incident beam by the polarization beam splitter and the $\lambda/4$ wave plate, and reflected onto the split photodiode.

In addition to the advantage of achieving a high imaging rate, small cantilevers have other advantages. The total thermal noise depends only on the spring constant and the temperature and is given by $\sqrt{k_B T/k_c}$, where k_B is Boltzmann's constant and T is the temperature in kelvins. Therefore, a cantilever with a higher resonant frequency has a lower noise density. In the tapping mode, the frequency region used for imaging is approximately the imaging bandwidth (its maximum is the feedback frequency) centered on the resonant frequency. Thus, a cantilever with a higher resonant frequency is less affected by thermal noise. In addition, shorter cantilevers have higher OBD detection sensitivity because the sensitivity is $\Delta\phi/\Delta z = 3/2L$, where Δz is the displacement and $\Delta\phi$ is the change in the angle of a free cantilever end. A high resonant frequency and a small spring constant result in a large ratio f_c/k_c , which gives the cantilever high sensitivity to the gradient k of the force exerted between the tip and the sample. The gradient of the force shifts the cantilever resonant frequency by approximately $-0.5kf_c/k_c$. Therefore, small cantilevers with large values of f_c/k_c are useful for phase-contrast imaging. The practice of phase-contrast imaging using small cantilevers is described in Section 17.5.5.

17.4.2. Tip–Sample Interaction Detection

Tip–sample interactions change the amplitude, phase, and resonant frequency of the oscillating cantilever. They also produce higher harmonic oscillations. In this section, we describe methods for detecting the amplitude and the interaction force. A fast detection method of phase shifts is described in Section 17.4.7.

Amplitude Detectors

Conventional RMS-to-DC converters require at least several oscillation cycles to output an accurate RMS value. To detect the cantilever oscillation amplitude at the periodicity of half the oscillation cycle, we developed a peak–hold method; the peak and bottom voltages are captured and then their difference is output as the amplitude (Figure 17.5) (Ando et al., 2001). The sample/hold timing signals are usually produced using the input signals [shown at (i) in Figure 17.5] (i.e., sensor output signals) themselves. Alternatively, external signals [shown at (ii) in Figure 17.5] that are synchronized with the cantilever excitation signals can be used to produce the timing signals. This is sometimes useful for maximizing the detection sensitivity of the tip–sample interaction because the detected signal is affected by both the amplitude change and the phase shift. This is the fastest amplitude detector, and the phase delay has a minimum value of π . A drawback of this amplitude detector seems to be the detection of noise because the sample/hold circuits capture the sensor signal only at two timing positions. However, the electric noise detected in this peak–hold method is less than that produced by the thermal fluctuations of the cantilever oscillation amplitude.

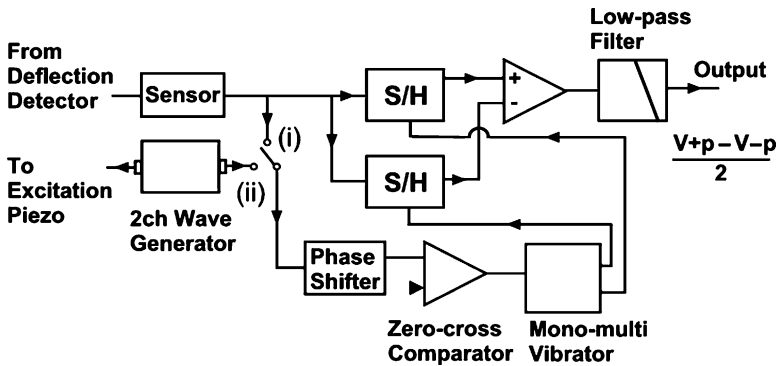


Figure 17.5. Circuit for fast amplitude measurement. The output sinusoidal signal from the split-photodiode amplifier is fed to this circuit. The output of this circuit provides the amplitude of the sinusoidal input signal at half the periodicity of the oscillation signal. 2ch; two-channel.

A different type of amplitude (plus phase) detector can be simply constructed using an analog multiplier and a low-pass filter. The sensor signal $s(t) \sim A_m(t) \sin[\omega_0 t + \varphi(t)]$ is multiplied by a reference signal $2 \sin(\omega_0 t + \phi)$ that is synchronized with the excitation signal. This multiplication produces a signal given by

$$A_m(t) \{ \cos [\varphi(t) - \phi] - \cos [2\omega_0 t + \varphi(t) + \phi] \} \quad (17.13)$$

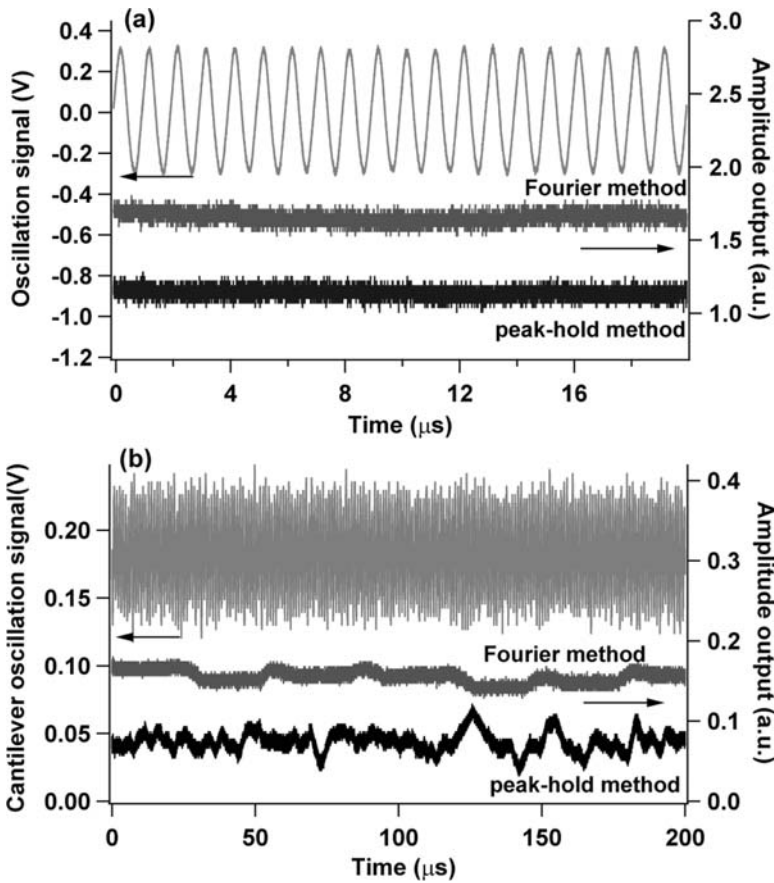


Figure 17.6. Noise levels of two amplitude detection methods (peak-hold method and Fourier method). The upper trace represents the input signal. (a) Electric noise. A clean sinusoidal signal mixed with white noise was input to the detectors. The root mean square voltage of white noise was adjusted to be the same magnitude as that of the optical beam deflection photensor output. (b) Variations in the detected cantilever oscillation amplitude.

By adjusting the phase of the reference signal and placing a low-pass filter after the multiplier output, we can obtain a DC signal of $\sim A_m(t) \cos[\Delta\varphi(t)]$, where $\Delta\varphi(t)$ is a phase shift produced by the tip-sample interaction. In this method, the delay in the amplitude detection is determined mostly by the low-pass filter. In addition, electric noise is effectively removed by the low-pass filter.

A Fourier method for generating the amplitude signal at the periodicity of a single oscillation cycle has been proposed (Kokavecz et al., 2006). In this method, the Fourier sine and cosine coefficients A and B are calculated for the fundamental frequency from the deflection signal to produce $\sqrt{A^2 + B^2}$. The electric noise level in the Fourier method is similar to that in the peak-hold method (Figure 17.6a). However, regarding the accuracy of amplitude detection, the performance of the Fourier method is better because the cantilever's thermal deflection fluctuations can be averaged in this method (Figure 17.6b).

Force Detectors

A physical quantity that affects the cantilever oscillation is not the force itself but the impulse (\sim peak force \times time over which the tip interacts with the sample). In the tapping mode, the interaction time is short (\sim one-tenth the oscillation period). Consequently, the peak force is relatively large and therefore must be a more sensitive indicator of the interaction than the amplitude change. The impulsive force $F(t)$ consists of harmonic components and therefore cannot be detected directly because the cantilever's flexural oscillation gain is lower at higher harmonic frequencies. $F(t)$ can be calculated from the cantilever's oscillation wave $z(t)$ by substituting $z(t)$ into the equation of cantilever motion and then subtracting the excitation signal (i.e., inverse determination problem) (Stark et al., 2002; Chang et al., 2004; Legleiter et al., 2006). To ensure that this method is effective, the cantilever oscillation signal with a wide bandwidth (at least up to $\sim 5f_c$) must be detected, and fast analog or digital calculation systems are necessary for converting $z(t)$ to $F(t)$. In addition, a fast peak-hold system is necessary to capture the peak force. We are now attempting to build a peak-force detection circuit with a real-time calculation capability.

Recently, a method of directly detecting the impulsive force was presented (Sahin, 2007; Sahin et al., 2007). The torsional vibrations of a cantilever have a higher fundamental resonant frequency (f_t) than that of flexural oscillations (f_c). Therefore, the gain of torsional vibrations excited by impulsive tip-sample interaction is maintained at ~ 1 over frequencies higher than f_c . Here, we assume that flexural oscillations are excited at a frequency of $\sim f_c$. To excite torsional vibrations effectively, "torsional harmonic cantilevers" with an off-axis tip have been introduced (Sahin, 2007; Sahin et al., 2007). Oscilloscope traces of torsional vibration signals indicated a time-resolved tip-sample force. We recently observed similar force signals using our small cantilevers with an EBD tip at an off-axis position near the free beam end. After we filtered out the f_c component from the sensor output, periodic force signals appeared clearly (Figure 17.7). To use the sensitive force signals for high-speed imaging, we again need a means of capturing the peak force or a real-time calculation system to obtain it.

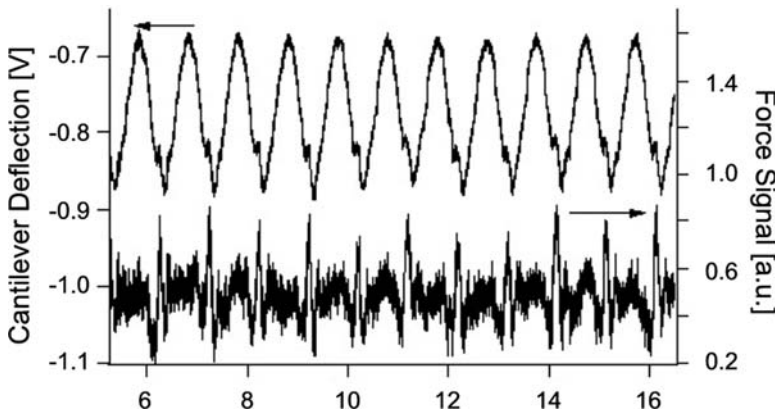


Figure 17.7. Force signal directly obtained from the torsional signal of a small cantilever with an off-axis tip. The cantilever was excited at its first flexural resonant frequency (~ 1 MHz) in water. The off-axis tip was intermittently contacted with a mica surface in water. The upper trace shows the torsional vibrations of the cantilever. The lower trace shows the force signal obtained by filtering the torsional signal using a low-pass filter to remove the carrier wave (1 MHz). The torsional signal appears even under free oscillation owing to cross-talk between flexural and torsional vibrations.

17.4.3. High-Speed Scanner

The high-speed driving of mechanical devices having macroscopic dimensions tends to produce unwanted vibrations. Therefore, among the devices used in high-speed AFM, the scanner is the most difficult to optimize for high-speed scanning. Several techniques are required to realize high-speed scanners: (1) a technique to suppress the structural vibrations, (2) a technique to increase the resonant frequencies, (3) an active damping technique to reduce the resonant vibrations of the piezoelectric actuators, and (4) a technique to attain small cross-talk between the three axes.

Counterbalance

The quick displacements of a piezoelectric actuator exert impulsive forces onto the supporting base, which cause vibrations of the base and the surrounding framework and, in turn, of the actuator itself. To alleviate the vibrations, a counterbalance method was introduced for the z -scanner (Ando et al., 2001); impulsive forces are countered by the simultaneous displacements of two z -piezoelectric actuators of the same length in the counter direction (Figure 17.8a). In this arrangement, which we are currently using, the counterbalance works effectively below the first resonant frequency of the piezoelectric actuators. Because the resonant frequencies originating in the scanner structure are generally lower than those of piezoelectric actuators, structural vibrations are almost completely suppressed. In the arrangement depicted in Figure 17.8a, we can use the maximum displacement of the piezoelectric actuator. However, the resonant frequency becomes approximately half the resonant frequency of the piezoelectric actuator under free oscillation.

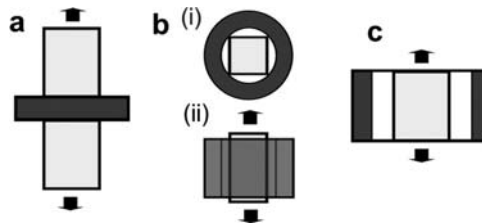


Figure 17.8. Various configurations of holding piezoelectric actuator for suppressing unwanted vibrations. The piezoelectric actuators are shown in light gray, and the holders are shown in black. **(a)** Two actuators are attached to the base. **(b)** An actuator is glued to the solid base at the rims parallel to the displacement direction, top (i) and side (ii) views. **(c)** The two ends of an actuator are held with flexures in the displacement direction.

Figure 17.8b shows a different counterbalance method that we recently developed (Fukuma et al., 2008). A piezoelectric actuator is glued to (or pushed into) a circular hole of a solid base so that the four side rims parallel to the displacement direction are held. Even when held in this way, the actuator can be displaced almost up to the maximum length attained under the load-free condition. In this method, the available maximum displacement becomes approximately half the maximum displacement of the piezoelectric actuator. However, the resonant frequency is almost unchanged from that under free oscillation. This method can also be used for the x - and y -scanners.

Figure 17.8c shows a counterbalance method that we are using for the x -scanner (although we will change it to the rim-holding method described earlier). A piezoelectric actuator is sandwiched between two flexures in the displacement directions. To ensure that

this method is effective, the flexure resonant frequency must be increased, and hence a large spring constant of the flexures must be used, which results in the reduction of the maximum displacement of the scanner.

Mechanical Scanner Design

The structural resonant frequency can be enhanced by adopting a compact structure and a material that has a large Young's modulus-to-density ratio. However, a compact structure tends to produce interference (cross-talk) among the three scan axes. To achieve small cross-talk, we can use flexures (blade springs) that are sufficiently flexible to be displaced but sufficiently rigid in the directions perpendicular to the displacement axis (Kindt et al., 2004; Ando et al., 2005). The scanner mechanism, except for the piezoelectric actuators, must be produced by monolithic processing to minimize the number of resonant elements. We have used an asymmetric structure in the x and y directions; the slowest y -scanner displaces the x -scanner, and the x -scanner displaces the z -scanner, as in our currently used scanner (Figure 17.9). With this scanner, the maximum displacements (at 100 V) of the x - and y -scanners are 1 and 3 μm , respectively. Two z -piezoelectric actuators (maximum displacement, 2 μm at 100 V; self-resonant frequency, 360 kHz) are used in the configuration shown in Figure 17.8a. The gaps in the scanner are filled with an elastomer to passively damp the vibrations. This passive damping is effective in suppressing low-frequency vibrations. To minimize the hydrodynamic pressure generated by the quick displacement of the z -scanner (Ando et al., 2002), we have been using glass sample stages with a circular-trapezoid (or pillar) shape and a small top surface of 1–2 mm diameter.

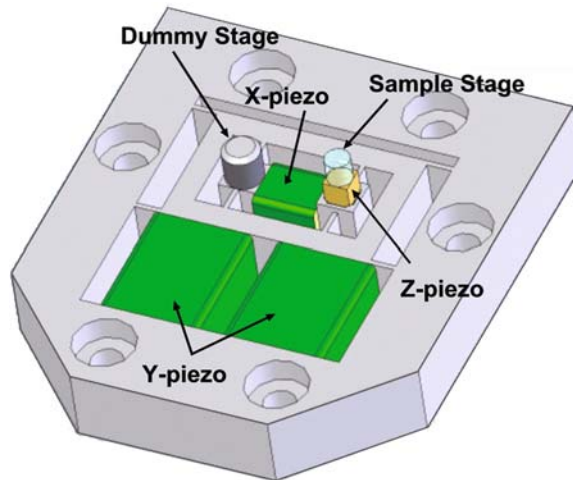


Figure 17.9. Sketch of the high-speed scanner currently used for imaging studies. A sample stage is attached at the top of the upper z -piezoelectric actuator (the lower z -piezoelectric actuator used for counterbalancing is hidden). The dimensions ($W \times L \times H$) of the z -actuators are $3 \times 3 \times 2 \text{ mm}^3$. The gaps are filled with an elastomer for passive damping.

17.4.4. Active Damping

As mentioned later, the most advanced high-speed scanner has the lowest resonant frequency of $\sim 500 \text{ kHz}$ and the maximum displacement of $\sim 1 \mu\text{m}$ in the z direction. Therefore, we do not need to expand much effort to actively damp the z -scanner vibrations because its

feedback scan (~150 kHz for video-rate imaging) would not excite the z-scanner resonance of such a high frequency. Here, we describe simple active damping techniques among those developed previously. Because notch filtering, which can be effectively used for eliminating a single clean resonance, is simple, it is not described here.

Feedback Q Control

In the feedback damping method (Figure 17.10a), the feedback operator $H(s)$ converts the resonant system $G(s)$ to a target system $R(s)$ expressed as

$$R(s) = \frac{G(s)}{1 - G(s)H(s)} \tag{17.14}$$

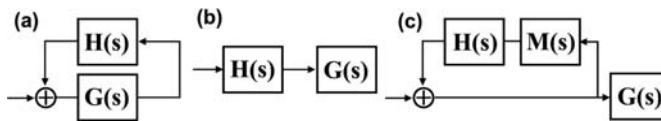


Figure 17.10. Active damping methods for suppressing the unwanted vibrations of the scanner. (a) Feedback control method. (b) Feedforward control method. (c) Feedback Q -control system with a mock scanner. $G(s)$ represents the transfer function of the scanner to be controlled, and $M(s)$ represents the transfer function of the mock scanner. $M(s)$ is similar to the transfer function $G(s)$. $H(s)$ represents the transfer function of the controller for active damping.

In the first step, let us consider the simplest case, where $G(s)$ consists of a single resonant element with resonant frequency ω_1 and quality factor Q_1 . The target system is expressed as a single resonator with resonant frequency ω_0 and quality factor Q_0 . For these systems, $H(s)$ is expressed as

$$H(s) = \frac{1}{G(s)} - \frac{1}{R(s)} = \left(\frac{s^2}{\omega_1^2} + \frac{s}{Q_1\omega_1} + 1 \right) - \left(\frac{s^2}{\omega_0^2} + \frac{s}{Q_0\omega_0} + 1 \right) \tag{17.15}$$

To eliminate the second-order term from $H(s)$, ω_0 should equal ω_1 , which results in

$$H(s) = - \left(\frac{1}{Q_0} - \frac{1}{Q_1} \right) \frac{s}{\omega_1} \tag{17.16}$$

This $H(s)$ is identical to a derivative operator with a gain of -1 at the frequency $\hat{\omega} = Q_0Q_1\omega_1/(Q_1 - Q_0)$. By adjusting the gain parameter of the derivative operator, we can arbitrarily change the target quality factor Q_0 . This method is known as “ Q -control” and is often used for controlling the quality factor of cantilevers (Anczykowski et al., 1998; Gao et al., 2001; Tamayo et al., 2001). Here, note that when the Q -controller is applied to the z-scanner, we must measure the displacement or velocity of the z-scanner. However, this is difficult. This problem is solved by using a mock scanner $M(s)$ (a second-order low-pass filter) characterized by the same transfer function as the z-scanner (Figure 17.10c) (Kodera et al., 2005). The practical use of this technique is described in the next section.

Real scanners often exhibit multiple resonant peaks, and therefore the simple Q control just described does not work well. When elemental resonators are connected in series, we must use mock scanners $M_1(s), M_2(s), \dots$, each of which is characterized by a transfer function representing each elemental resonator. Each mock scanner is controlled by a corresponding

Q -controller. For example, when the scanner consists of two resonators connected in series, the composite transfer function $T(s)$ of the total system is expressed as

$$T(s) = \frac{1}{1 - M_1(s)H_1(s)} \times \frac{1}{1 - M_2(s)H_2(s)} \times G_1(s)G_2(s) \quad (17.17)$$

Because $M_1(s)$ and $M_2(s)$ are the same as (or similar to) $G_1(s)$ and $G_2(s)$, respectively, Eq. (17.17) represents a target system consisting of damped resonators connected in series.

When the scanner consists of elemental resonators connected in parallel, active damping becomes more difficult. Although it does not work perfectly, we can use a mock scanner with two resonators connected in parallel. This gives a better result compared with the case in which the mock scanner with a single resonator is used. More sophisticated methods are described elsewhere (Ando et al., 2008b).

Feedforward Active Damping

The feedforward control type of active damping (Figure 17.10b) is based on inverse compensation [i.e., $H(s) \sim 1/G(s)$]. Generally, inverse compensation-based damping has an advantage, in that we can extend the scanner bandwidth. This damping method is much easier to apply for the x -scanner than for the z -scanner because for the former, the scan waves are known beforehand and are periodic (hence, the frequencies used are discrete, integral multiples of the fundamental frequency) (Schitter et al., 2004; Hung et al., 2006). Here, we only describe the damping of the x -scanner vibrations. The waveforms of the x -scan (as a function of time) are isosceles triangles characterized by amplitude X_0 and fundamental angular frequency ω_0 . Their Fourier transform is given by

$$F(\omega) = 2\pi X_0 \left[\frac{1}{2} \delta(\omega) - \frac{2}{\pi^2} \sum_{k=-\infty}^{+\infty} \frac{1}{k^2} \delta(\omega - k\omega_0) \right] \quad (k: \text{odd}) \quad (17.18)$$

To move the x -scanner in the isosceles triangle waveforms, the signal $X(t)$, which drives the x -scanner characterized by the transfer function $G(s)$, is given by the inverse Fourier transform of $F(\omega)/G(i\omega)$, and is expressed as

$$X(t) = \frac{X_0}{2} - \frac{4X_0}{\pi^2} \sum_{k=1}^{+\infty} \frac{1}{k^2} \frac{1}{G(ik\omega_0)} \cos(k\omega_0 t) \quad (k: \text{odd}) \quad (17.19)$$

In practice, the sum of the first ~ 10 terms in the series of Eq. (17.19) is sufficient. We can calculate Eq. (17.19) in advance to obtain numerical values of $X(t)$ and output them in succession from a computer through a D/A converter.

Practice of Active Damping of the Scanner

In this section, we describe the active damping applied to the scanners that we are currently using (one type is shown in Figure 17.9) and to another scanner under development. Here, we first show the effect of feedforward active damping applied to the x -scanner having a large resonance at ~ 60 kHz. When the line scan was performed at 3.3 kHz without damping, its displacement exhibited vibrations (Figure 17.11a). When it was driven by a waveform

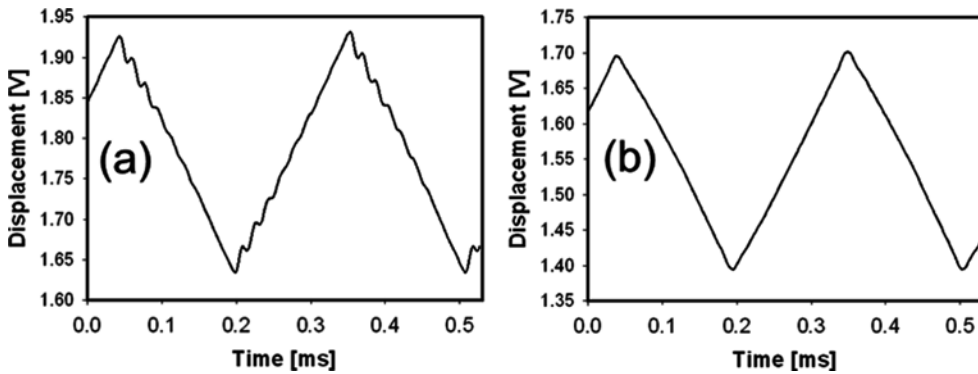


Figure 17.11. Effect of feedforward active-damping control on the x -scanner vibrations. (a) The x -scanner displacement driven by triangular waves without damping. (b) The x -scanner displacement driven by triangular waves compensated by feedforward control.

calculated using Eq. (17.19) with the maximum term $k = 17$ in the series, the x -scanner moved approximately in the isosceles triangle waveform (Figure 17.11b).

In the z -scanner that we are currently using for imaging studies, the z -piezoelectric actuators have a resonant frequency of 410 kHz under free oscillation. The counterbalance method employed is depicted in Figure 17.8a. With this method of counterbalancing, no structural resonances appear at frequencies lower than the first resonant frequency (171 kHz) of the two identical z -piezoelectric actuators (gray lines in Figure 17.12). The resonant frequency of 171 kHz is derived from the fact that one end of each piezoelectric actuator is attached to the base ($410/2 = 205$ kHz) and the other end is attached to a sample stage (or a dummy stage). Higher resonant frequencies also appear at around 350 kHz. Judging from the phase spectrum (gray line in Figure 17.12b), the two main resonant elements are connected in parallel. For the active damping of these resonant vibrations, we employ the simple Q -control method (Figure 17.10c) described in the subsection Feedback Q Control. In addition, to compensate for the phase delay produced by active damping, a $(1 + \text{derivative})$ circuit is inserted between the Q -controller and the piezodriver. Although this method does not work perfectly, we use a mock z -scanner with two resonator circuits connected in parallel. With this method of Q control, the first resonance completely disappears (the black line in Figure 17.12a), and the phase delay is not significantly deteriorated (the black line in Figure 17.12b). Because the quality factor is reduced significantly, the z -scanner response time is markedly improved, from $17.1 \mu\text{s}$ to $0.93 \mu\text{s}$ (Figure 17.13). The slight ringing observed at the rising and falling edges are due to the remaining resonances at around 350 kHz. These resonances could be removed using a notch filter or a low-pass filter, but we do not remove them because such filtering increases the phase delay. In practice, these remaining resonances negligibly disturb the imaging of protein molecules, even at an imaging rate of 30 ms/frame over a scan range of 240 nm with 100 scan lines.

We recently attempted to develop other types of scanners in which a z -piezoelectric actuator is held at the four side rims parallel to the displacement direction (Fukuma et al., 2008) (method depicted in Figure 17.8b). The gain and phase spectra of the mechanical response of the z -scanner are shown by the black lines in Figures 17.14a, b. The z -scanner exhibited large resonant peaks at 440 and 550 kHz. The resonant frequency of 440 kHz is very similar to that of the free oscillation of the piezoelectric actuator. Judging from the

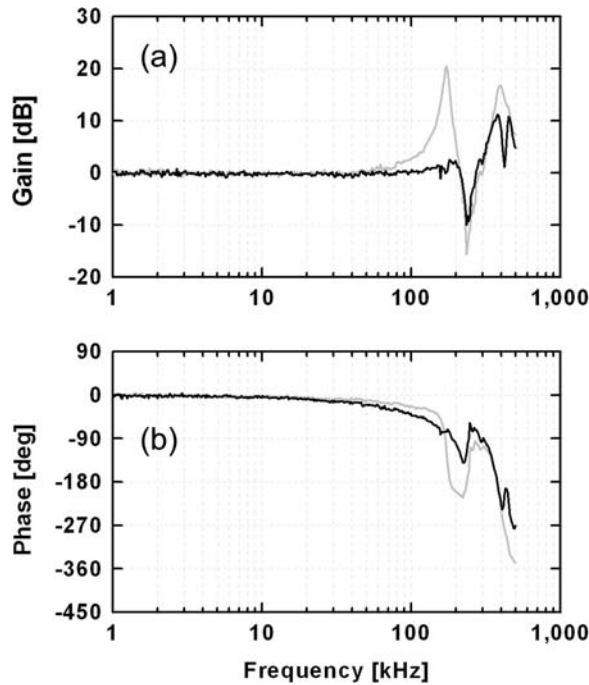


Figure 17.12. Frequency spectra of mechanical response of the z-scanner. (a) Gain spectra. (b) Phase spectra. Gray lines represent the response without feedback Q control, and black lines represent the response with feedback Q control.

phase spectrum, the two resonators are connected in series. We used two active Q -control circuits connected in series [see Eq. (17.17)]. The resulting gain and phase spectra are shown by the gray lines in Figures 14a, b, respectively. The peak at 440 kHz is almost completely removed, and the frequency that gives a 90° phase delay reaches 250 kHz.

17.4.5. Dynamic PID Control

Dynamic PID Controller

Various efforts have been made to increase the AFM scan speed. However, little attention has been directed toward reducing the tip-sample interaction force. This reduction is quite important for biological AFM imaging. The most ideal scheme is the use of noncontact AFM (nc-AFM), but, to date, high-speed nc-AFM has not been exploited. It is unknown whether the high-speed and noncontact conditions can be reconciled with each other. We previously discussed this matter (Ando et al., 2008a, b). There are several methods of reducing the force in tapping-mode AFM: (1) use of softer cantilevers, (2) enhancement of the quality factor of small cantilevers, and (3) use of a shallower amplitude set-point (i.e., r is close to 1). However, none of these methods appears to be compatible with high-speed scanning. The most advanced small cantilevers developed seem to have reached their limit of balancing high resonant frequency with a small spring constant, and, hence, softer cantilevers can

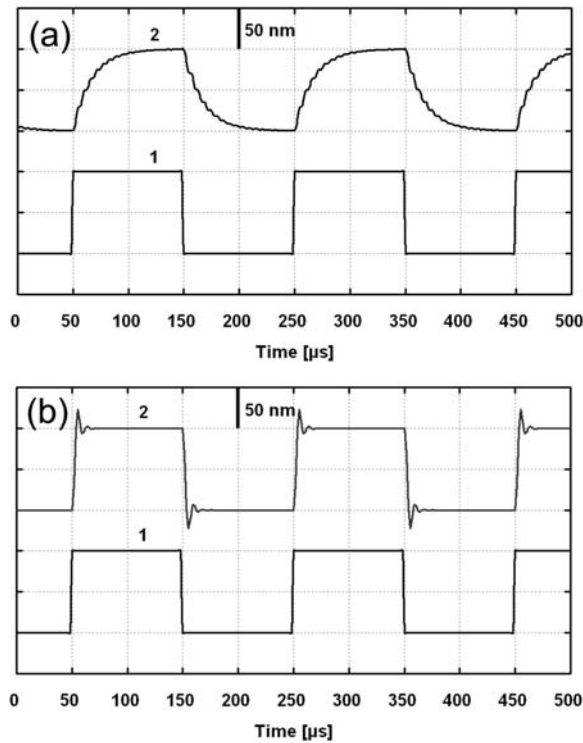


Figure 17.13. Cantilever deflection responses to rectangular variation of the set-point of the proportional integral derivative controller. (a) Trace 2 is obtained without active damping of the z -scanner vibrations. (b) Trace 2 is obtained with active damping. Traces 1 represent the rectangular set-point variation.

be obtained only by sacrificing the resonant frequency. Although the tapping force decreases with increasing Q in the cantilever, so does its response speed.

The last possibility—a shallower amplitude set-point—promotes “parachuting” during which the error signal is saturated at $2A_0(1 - r)$, and therefore the parachuting time is prolonged with increasing r , resulting in a decrease in the feedback bandwidth. This difficult issue was resolved by the invention of a new PID controller, the “dynamic PID controller,” whose gains are automatically changed depending on the cantilever’s oscillation amplitude (Kodera et al., 2006). Briefly, a threshold level A_{upper} is set at or slightly above the set-point amplitude $A_s = 2A_0r$. When the cantilever peak-to-peak oscillation amplitude $A_{\text{p-p}}$ exceeds this threshold level, the feedback gain is increased, which either shortens the parachuting time or avoids parachuting entirely. As mentioned in the next section, the dynamic PID controller can avoid parachuting even when r is increased to ~ 0.9 . Note that to ensure that this dynamic PID controller is effective even when the set-point r is very close to 1, the amplitude signal should not contain noise greater than $\sim 2A_0(1 - r)/3$.

Similar manipulation of the error signal can also be performed when $A_{\text{p-p}}$ is smaller than A_s . In this case, a new threshold level A_{lower} is set with a value sufficiently lower than A_s . When $A_{\text{p-p}}$ becomes lower than A_{lower} , the feedback gain is increased. This can prevent the cantilever tip from pushing into the sample too strongly, particularly at steep uphill regions of the sample.

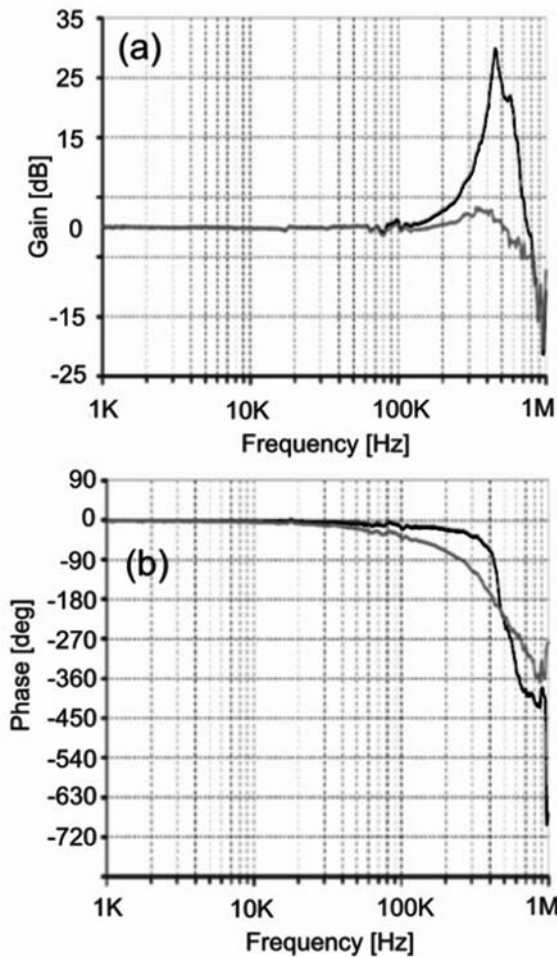


Figure 17.14. Frequency spectra of the mechanical response of the z -scanner. **(a)**, **(b)**. The gain and phase spectra, respectively, of a z -scanner whose piezoelectric actuator is held at the four rims parallel to the displacement direction (see Figure 17.8b). Black lines represent the responses without feedforward active damping, and gray lines represent the responses with feedback Q control.

Performance of Dynamic PID Control

Dynamic PID control significantly enhances the feedback bandwidth, particularly when the set-point r is close to 1 (dotted curves in Figure 17.15). The feedback bandwidth becomes independent of r , provided r is less than ~ 0.9 , indicating that parachuting does not occur. The superiority of the dynamic PID control is also clear from captured images of a mock sample with steep slopes (Figure 17.16a). The images were obtained using a mock AFM. Here, a mock cantilever with $Q = 3$ oscillating at its resonant frequency of 1.2 MHz is scanned over a mock sample surface (rectangular shapes with two different heights) from left to right at a scan speed of 1 mm/sec (frame rate of 100 ms/frame). Here, the height of the taller rectangle is $2A_0$, and A_s is set at $0.9 \times 2A_0$. When the conventional PID controller was used,

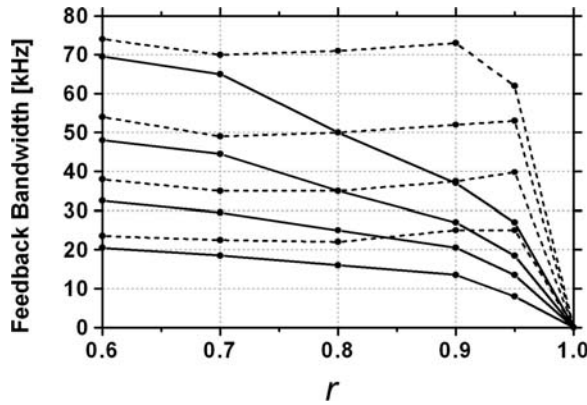


Figure 17.15. Feedback bandwidth as a function of the set-point r , measured using the mock atomic force microscope (AFM) system. The solid curves show the feedback bandwidths measured using the mock AFM system with a conventional proportional integral derivative (PID) controller. The dotted curves show the feedback bandwidths measured using the mock AFM system with the dynamic PID controller. The solid curves and the dotted curves are aligned from top to bottom according to the ratio $2A_0/h_0 = 5, 2, 1, \text{ and } 0.5$, respectively.

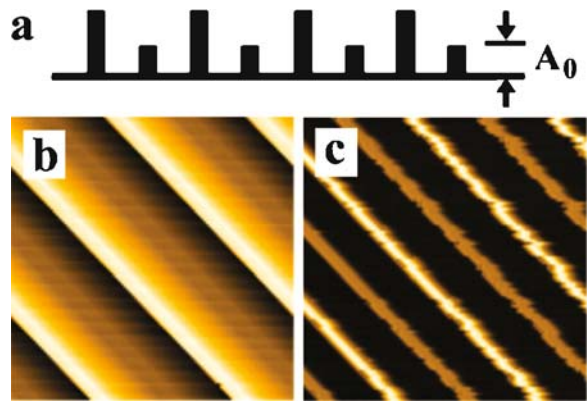


Figure 17.16. Pseudo-atomic force microscope (AFM) images of a sample with rectangles of two different heights. (a) Mock AFM sample. (b), (c) The images were obtained using a conventional proportional integral derivative (PID) controller and the dynamic PID controller, respectively. The simulations with the mock AFM system were performed under the following conditions: cantilever resonant frequency, 1.2 MHz; quality factor of cantilever oscillation, 3; resonant frequency of z -scanner, 150 kHz; quality factor of z -scanner, 0.5; line scan speed, 1 mm/sec; line scan frequency, 1 kHz; frame rate, 100 ms/frame; ratio of $2A_0$ to total sample height, 1; and $r = 0.9$

the topographic image became blurred (Figure 17.16b) due to significant parachuting at steep downhill regions. On the other hand, the use of the dynamic PID controller resulted in a clear image (Figure 17.16c), indicating that almost no parachuting occurred. Dynamic PID control improves both the feedback bandwidth and the tapping force simultaneously and is therefore indispensable in the high-speed AFM imaging of delicate samples.

17.4.6. Drift Compensator

The drift in the cantilever excitation efficiency poses a problem, particularly when r is close to 1 (i.e., A_s is set close to $2A_0$). For example, as the efficiency is lowered, $2A_0$ decreases and, concomitantly, A_{p-p} decreases. The feedback system interprets this decrease in A_{p-p} as an overly strong interaction of the tip with the sample and therefore withdraws the sample stage from the cantilever; this is an incorrect operation. This withdrawal tends to dissociate the cantilever tip completely from the sample surface. For example, when $2A_0 = 5$ nm and $A_s = 4.5$ nm ($r = 0.9$), their difference is only 0.5 nm. The satisfactory operation of dynamic PID control under such a set-point condition requires high stability of the excitation efficiency. The stabilization of the excitation efficiency was previously attempted (Schiener et al., 2004) by using the second-harmonic amplitude of the cantilever oscillation to detect drifts. The second-harmonic amplitude is sensitive to the tip-sample interaction, and therefore the drift in A_0 is reflected in the second-harmonic amplitude averaged over a period longer than the image-acquisition time. To compensate for drift in the cantilever excitation efficiency, we also used the second-harmonic amplitude of cantilever oscillation, but instead of controlling A_s , we controlled the output gain of a wave generator (WF-1946A, NF Corp., Osaka, Japan) connected to the excitation piezoelectric actuator (Kodera et al., 2006). We only used an I-controller whose time constant was adjusted to 1–2 sec (about ten times longer than the image acquisition time). By this drift compensation method, we achieved very stable imaging, even with a small difference ($2A_0 - A_s$) of 0.4 nm.

17.4.7. High-Speed Phase Detector

The material property map is obtained by measuring the phase difference between the excitation signal and the cantilever oscillation (Tamayo and Garcia, 1996; Bar et al., 1997; Cleveland et al., 1998). The phase difference is related to several material properties, such as viscoelasticity, elasticity, adhesion, hydrophobicity/hydrophilicity (Tamayo and Garcia, 1996), and surface charge (Czajkowsky et al., 1998). The energy dissipation of an oscillating cantilever due to inelastic tip-sample interactions is considered to be the main mechanism in the generation of phase contrast (Cleveland et al., 1998). Combining the information on these properties with a topographic video image with unprecedented temporal resolution would provide a deeper insight into biomolecular functional mechanisms and dynamic processes.

For high-speed phase-contrast imaging, we need a fast phase detector. As mentioned in Section 17.4.1, the cantilever resonant frequency shifts by approximately $-0.5kf_c/k_c$ by energy-conservative tip-sample interaction. The frequency shift results in a phase shift as the excitation frequency is fixed. For a given frequency shift, the phase shift increases with Q . With conventional cantilevers, the frequency shift is generally around 50 Hz. Therefore, phase-contrast imaging had been possible only with a large Q (hence only at a low imaging rate). Because the ratio f_c/k_c with the most advanced small cantilevers is $\sim 1,000$ times larger than that with conventional cantilevers, we can expect a large shift of ~ 50 kHz. Therefore, even with a small Q , a relatively large phase shift occurs. Even in the energy-dissipative tip-sample interaction, we can expect a large phase shift with small cantilevers because of a relatively small damping effect of the surrounding medium. Thus, we do not need to detect the phase shift using a very sensitive yet slow phase detector such as a lock-in amplifier. To explore the possibility of high-speed phase-contrast imaging, a fast phase detector was developed (Uchihashi et al., 2006) on the basis of a previous design (Stark and Guckenberger, 1999). Figure 17.17 shows the operational principle of the fast phase detection. A two-channel

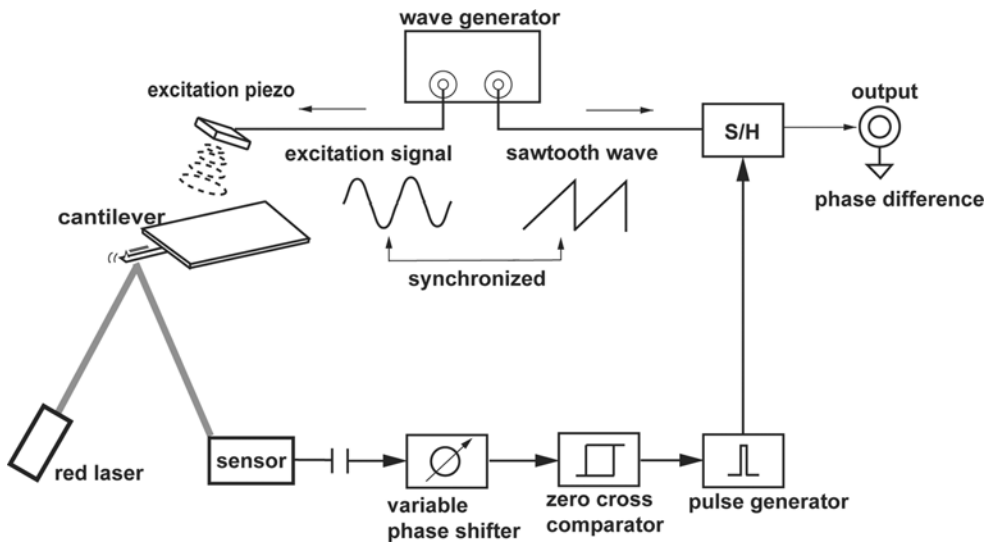


Figure 17.17. Schematic diagram of the fast phase-detection system for the atomic force microscope. S/H, sample-and-hold.

waveform generator produces sinusoidal and sawtooth waves with a given phase difference. The sinusoidal wave is used to oscillate the cantilever. The cantilever oscillation signal is fed to a phase detector composed of a high-pass filter, a variable phase shifter, a zero-crossing comparator, a pulse generator, and a sample-and-hold (S/H) circuit. A pulse signal is generated at either the rising or falling edge of the output signal of the zero-crossing comparator. The pulse signal acts as a trigger for the S/H circuit. When the trigger is generated, the amplitude voltage of the sawtooth signal is captured and retained by the S/H circuit. Thus, the sawtooth signal acts as a phase-voltage converter. The variable phase shifter enables us to vary the timing of the trigger signal generated within the cantilever oscillation cycle. This function is essential for obtaining the optimum phase contrast because the phase contrast markedly depends on the trigger timing, as will be described in Section 17.5.5.

The bandwidth of the fast phase detector reached 1.3 MHz. However, its sensitivity was not as high as that of a lock-in amplifier. The main noise source of the fast phase detector is jitter originating from voltage noise contained in the PSPD output. The RMS value of jitter Δt_{RMS} for a sinusoidal wave containing broadband white noise V_{RMS} is given by

$$\Delta t_{RMS} = \frac{V_{RMS}}{2\pi A f_{osc}} \tag{17.20}$$

Here, A and f_{osc} are the amplitude and frequency of the sinusoidal wave, respectively. The jitter gives rise to timing fluctuations in the trigger pulse for the S/H circuit, and therefore the phase error ΔP_{RMS} (in degrees) is given by

$$\Delta P_{RMS} = \frac{V_{RMS}}{2\pi A} \times 360^\circ = \frac{360^\circ}{2\pi \times SNR} \tag{17.21}$$

where SNR is the signal-to-noise ratio of the sensor output (i.e., A/V_{RMS}). In the actual experiment, $\text{SNR} < 10$ due to the thermal fluctuations of the cantilever under a low- Q condition. Therefore, the intrinsic phase noise is expected to be larger than 5.7° . However, because the bandwidth of 1.3 MHz is much higher than the imaging bandwidth (approximately 100 kHz), the phase noise can be reduced by using a low-pass filter.

17.5. High-Speed Bioimaging

High-speed AFM imaging studies performed thus far are classified into three categories: early, middle period, and recent studies. In the early stage, imaging studies were carried out to find devices and techniques to be improved. The most serious obstacle we encountered in this stage was that the tip-sample interaction was too strong. Fragile samples such as microtubules and actin filaments were destroyed during imaging. This was due not only to the insufficient feedback speed, but also to the large tapping force exerted by the oscillating tip on the sample. A prototype dynamic PID controller (Ando et al., 2003) and an active damping technique for the z -scanner (Kodera et al., 2005) were developed during this period. Using the dynamic PID controller, the tapping force was greatly reduced and the feedback bandwidth was enhanced. For example, the unidirectional movement of individual kinesin molecules along microtubules was observed without disassembling the microtubules (Ando et al., 2003).

In the middle period, imaging studies were performed to confirm whether biological processes that had been known or predicted to occur would indeed be visualized. For example, the gliding movement of actin filaments over a surface densely coated with myosin V was captured on video (Ando et al., 2005; 2006). However, when the myosin V density was lowered, actin filaments did not appear in the images, suggesting that they were removed by the scanning and oscillating tip. Another example is the stem movement of dynein C in the presence of adenosine triphosphate (ATP). The video image revealed that the stem moved back and forth between two positions while the stalk and head remained stationary (Ando et al., 2005; 2006). The two positions approximately corresponded to the nucleotide-free and adenosine diphosphate (ADP)-vanadate bound states (Burgess et al., 2003). In this period, we developed a method of combining flash photolysis of caged compounds with high-speed AFM. Attenuated high-frequency laser pulses (~ 50 kHz, 355 nm) were applied while the y -scan was performed toward the starting point after the completion of one frame acquisition. During this y -scan period, the sample stage was withdrawn from the cantilever tip. This method allowed us to observe the rotational movement of the myosin V head around the head-neck junction that occurred immediately after ultraviolet application to the caged ATP-containing solution (Ando et al., 2006). We also applied this method to observe the height changes in chaperonin GroEL on binding to ATP and GroES (Ando et al., 2005; 2006).

More recently, full-scale imaging studies have been carried out to explore the potential of high-speed AFM, some of which have proved that the current state of our high-speed AFM can be used to reveal functional mechanisms of proteins, although further improvements are still necessary, particularly on the reduction in the tip-sample interaction force. In the following sections, we describe some recent imaging studies.

17.5.1. Chaperonin GroEL

Here, we show that a long-lasting controversial question regarding a biomolecular reaction was quickly solved by directly observing the reaction dynamics. Chaperonin GroEL

consists of 14 identical ATPase subunits that form two heptameric rings stacked back to back (Braig et al., 1994; Xu et al., 1997). A series of biochemical studies (e.g., Burston et al., 1995; Yifrach and Horovitz, 1995) showed that there is positive cooperativity regarding the binding and hydrolysis of ATP in the same ring, whereas there is negative cooperativity between the two rings. Owing to this negative cooperativity, it has been presumed that GroEL binds to GroES at one ring while releasing GroES from the other (Lorimer, 1997; Rye et al., 1997; 1999). This alternate on–off switching appears to exclude the concomitant binding of GroES to both rings of GroEL. However, this issue had remained controversial (e.g., Azem et al., 1994; Grallert and Buchner, 2001) because some electron micrographs showed a complex of GroES–GroEL–GroES with a football shape. To place GroEL on a substratum in a side-on orientation so that both rings are accessible to GroES, we prepared GroEL biotinylated at the equatorial domains (Taguchi et al., 2001). GroEL was attached to streptavidin two-dimensional (2D) crystal sheets prepared on planar lipid bilayers containing a biotin lipid. We were able to capture the GroES alternate association and dissociation at the two GroEL rings. Surprisingly, before the alternate switching took place, a football structure appeared with a high probability (unpublished data). Thus, the high-speed AFM observation clearly solved the controversial issue.

17.5.2. Lattice Defect Diffusion in Two-Dimensional Protein Crystals

For protein crystal formation, the protein–protein association energy must be in an appropriate range. However, the association energy at each contact point had not been assessed experimentally. Here, we show that high-speed AFM imaging can enable its estimation. During protein crystal growth, vacancy point defects are sometimes formed. When their size is small, particularly in the case of monovacancy point defects, they cannot be easily filled with protein molecules floating in the bulk solution. Consequently, they must remain in the crystal. However, in reality, they are mostly removed. Here, we show that high-speed AFM imaging can reveal the defect-removal mechanism.

As mentioned in the previous section, to observe GroEL–GroES association/dissociation dynamics, we prepared streptavidin 2D crystals on supported planar lipid bilayers (Darst et al., 1991). When we observed the crystal surfaces with orthorhombic *C*222 symmetry, we noticed that lattice defects sometimes formed at a few places and moved in the crystal (Figure 17.18). This movement is caused by exchanges between the defect (empty) site and one of the surrounding filled sites, because no free streptavidin exists in the bulk solution. To study the vacancy defect mobility and its participation in the crystal growth, monovacancy defects in the streptavidin 2D crystals were systematically produced by increasing the tapping

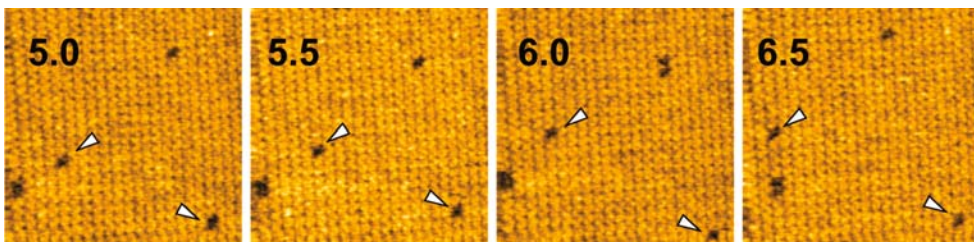


Figure 17.18. Movement of point defects in two-dimensional streptavidin crystal formed on a supported lipid planar bilayer containing biotinylated lipid. The point defects indicated by arrowheads are maintained as point defects during the observation. Scan range, 150 nm; imaging rate, 0.5 sec/frame.

force onto the sample from the oscillating tip. Unexpectedly, the movement of the created monovacancy defects had a preference for one direction over the other (Yamamoto et al., 2008). The movement projected onto each lattice axis showed a time–displacement relationship characteristic of Brownian motion, but the diffusion coefficients differed, depending on the axes.

Streptavidin is a homotetramer with subunits organized in dihedral D_2 symmetry. Therefore, in the 2D crystals, biotin only binds to the two subunits facing the planar lipid bilayers (Figure 17.19a). There are two types of subunit–subunit interactions between adjacent streptavidin molecules: interactions between biotin-bound subunits and interactions between biotin-unbound subunits (Figure 17.19b). One crystallographic axis (a axis) is comprised of contiguous biotin-bound subunit pairs, whereas the other axis (b axis) is comprised of contiguous biotin-unbound subunit pairs. A previous study on the formation of streptavidin 2D crystal on supported planar lipid bilayers suggested that the interaction between biotin-unbound subunits is stronger than that between biotin-bound subunits (Ku et al., 1993), whereas another study suggested the reverse relationship (Wang et al., 1999). For a streptavidin molecule to move to the adjacent monovacancy defect site along the a axis, two biotin-free subunit–subunit contacts and one biotin-bound subunit–subunit contact must be broken. On the other hand, to move along the b axis, two biotin-bound subunit–subunit contacts and one biotin-free subunit–subunit contact must be broken. Therefore, the preferential diffusion of the monovacancy defects along the b axis indicates that the association between biotin-bound subunits is weaker than that between biotin-free subunits. In addition, from the diffusion constant ratio ($D_b/D_a \sim 2.4$), the difference in the association free energy of the two types of subunit–subunit contacts (G_{u-u} and G_{b-b} for the biotin-unbound and biotin-bound pairs, respectively) are quantified to be $G_{u-u} - G_{b-b} \sim -0.88k_B T$ ($T \sim 300$ K), which corresponds to -0.52 kcal/mol (Yamamoto et al., 2008). The aspect ratio of the streptavidin C222 crystal is known to be ~ 2 at neutral pH (Yatcilla et al., 1998). Supposing that the aspect ratio of a crystal is proportional to the ratio of the free energies of attractive interactions that occur along the crystal axes [Wolff's rule (Wulff, 1901)], we find that G_{u-u}/G_{b-b} is approximately 2. This relationship and $G_{u-u} - G_{b-b} \sim -0.88k_B T$ result in $G_{b-b} \sim -0.88k_B T$ and $G_{u-u} \sim -1.76k_B T$.

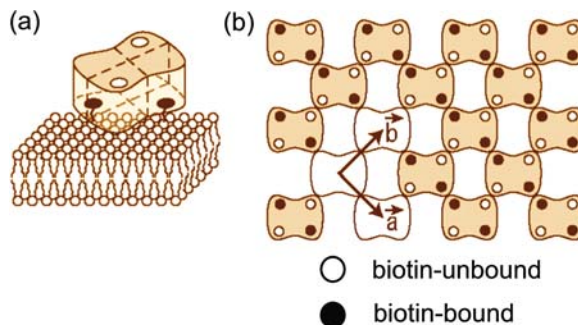


Figure 17.19. (a) Schematic of a streptavidin molecule on biotinylated lipid bilayer. Two biotin-binding sites occupied by biotin are indicated by the closed circles. The open circles indicate biotin-binding sites facing the aqueous solution and are biotin-free. (b) Schematic of streptavidin arrays in C222 crystal. Unit lattice vectors are indicated. The a axis includes rows of contiguous biotin-bound subunits, whereas the b axis includes rows of contiguous biotin-unbound subunits.

The fusion of two point defects into a larger point defect was often observed. On the other hand, the fission of a multivacancy point defect into smaller point defects was rarely observed (Yamamoto et al., 2008). We believe that fission often occurs but cannot easily be observed because the two point defects formed immediately after fission are quickly fused again. During the formation of streptavidin 2D crystals in the presence of free streptavidin in the bulk solution, small point defects such as mono- and divacancy defects do not have easy access to the free streptavidin molecules and hence have a tendency to remain in the crystals (Figure 17.20a). However, the fusion of small point defects into a larger point defect facilitates its access to the free streptavidin molecules and thereby promotes the removal of small point defects from the crystals (Figure 17.20b). Of interest, the defect mobility increases with increasing defect size (Yamamoto et al., 2008). The higher mobility of larger point defects increases their probability to encounter other point defects to form yet larger point defects with further higher mobility. During the crystal growth in the presence of free streptavidin in the bulk solution, this acceleration effect also promotes the removal of point defects from the crystalline regions.

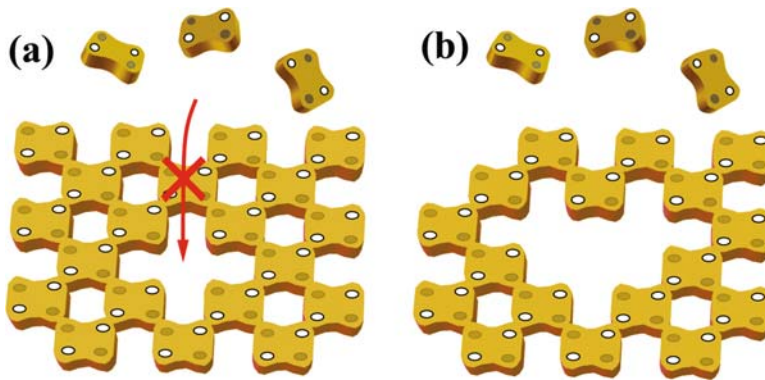


Figure 17.20. Filling vacancy defects in streptavidin two-dimensional crystal with free streptavidin molecules in the bulk solution. Small point defects (a) such as mono- and divacancy defects are not easily accessible the free streptavidin molecules, whereas larger point defects (b) are easily accessible to them and hence are removed from the crystal.

17.5.3. Myosin V

Here, we show that lively dynamic behavior of a motor protein can be captured by high-speed AFM. Myosin V is a double-headed, actin-based molecular motor that functions as an organelle transporter in various cells and moves processively along actin tracks (Sakamoto et al., 2000). After attaching to an actin filament, it can move on the actin filament over a long distance without dissociation. By single-molecule fluorescence microscopy studies, it has been established that the movement proceeds in 36-nm steps and in a hand-over-hand fashion (Yildiz et al., 2003; Forkey et al., 2003; Warshaw et al., 2005; Syed et al., 2006); the two heads alternate between the leading and trailing positions.

In physiological-ionic-strength solutions, myosin V tended to attach to the mica surface. In higher-ionic-strength solutions, it mostly remained free from the surface, but the affinity of myosin V for actin was lowered. To circumvent this problem, we reduced the cantilever free oscillation amplitude from the usual ~ 5 nm to ~ 1 nm, thereby reducing the tip-sample

interaction force but sacrificing the feedback bandwidth. With such small amplitude and in a high-ionic-strength solution containing a low concentration of ATP, the processive movement of myosin V was captured on video at 0.1 sec/frame. The two heads of a myosin V molecule alternated between leading and trailing positions with a walking stride of ~ 72 nm, that is, in a hand-over-hand manner (unpublished data). High-speed AFM revealed the movement in greater detail than fluorescence microscopy. The lead lever arm bent immediately before the rear head detached from the actin filament. This bent form was similar to that shown previously by electron microscopy (Burgess et al., 2002). The detached rear head rotated around the junction between the two lever arms and then attached to a frontward actin. Immediately after the attachment, the new lead head hopped and sometimes moved forward or backward by 5–10 nm along the actin filament. In the absence of nucleotide or in the presence of ADP, only one head of a myosin V molecule attached to an actin filament. From the orientation of the bound head, it was clear that the bound head was in the trailing position. On the other hand, in the presence of a medium concentration of adenylyl-imidodiphosphate (AMP-PNP), both heads were associated with an actin filament for a long time. This indicates that on binding to AMP-PNP, the lead head conformation adapts itself so that it is able to bind to actin by rotating around the head–neck junction. Therefore, when myosin V is bound to an actin filament at both heads in an ATP-containing solution, the trailing head must contain ADP (or no nucleotide at a low ATP concentration) and the lead head must contain ATP or ADP–inorganic phosphate. After the phosphate is released, the lead head rotates back to the previous orientation, which is unfavorable for actin binding. However, the lead head cannot dissociate from the actin because, in the ADP-bound state, the head has a high affinity for actin. This energetically unfavorable conformation causes the lead neck to bend forward, thereby pulling the trailing head, so that it detaches from the actin and is then conveyed forward. By these mechanical processes along the chemical reaction pathway, the two heads alternate their positions to walk along an actin filament.

17.5.4. Intrinsically Disordered Regions of Proteins

Here, we show that high-speed AFM imaging also is useful for identifying structurally flexible regions of proteins.

Biomolecular binding specificity had been described for a quite while by the famous “lock and key” mechanism, which postulated that a protein must be folded to give a high degree of geometrical precision in molecular binding. This concept has recently been overturned by a surprising yet credible finding that many proteins in the cell appear to be unfolded most of the time. Unstructured segments mostly comprise flexible linkers that play important roles in the assembly of macromolecular complexes and in the recognition of smaller biomolecules. The functional importance of intrinsically disordered (ID) regions has recently been recognized, particularly in transcription, translation, and cellular signal transduction (Demarest et al., 2002; Minezaki et al., 2006). However, there are no useful techniques for analyzing unstructured segments of this sort at the single-molecule level. Indeed, X-ray crystallography and electron microscopy do not allow the direct observation of the ID regions. Conventional slow AFM also cannot reveal such a thin and flexible entity. Under ambient conditions, thin and flexible unstructured polypeptides tend to form lumps or become flattened due to their strong attachment to a surface. Such flattened polypeptides are difficult to visualize by AFM. In addition, they are not easily adsorbed onto substrate surfaces in solution, even with the assistance of adhesive chemicals. Recently, we observed the facilitates chromatin transcription (FACT) protein in solution by high-speed AFM (Miyagi et al., 2008).

FACT is a heterodimer and displaces histone H2A/H2B dimers from nucleosomes, thereby facilitating RNA polymerase II transcription (Belotserkovskaya et al., 2003; Reinberg and Sims, 2006) and chromatin remodeling (Shimojima et al, 2003). The image of oligomerized FACT clearly revealed undulating tail-like structures protruding from the main body of FACT (Figure 17.21). The image of a FACT monomer indicated that FACT contains two tail-like structures of different lengths. This finding coincided with the ID regions predicted from the amino acid sequences. In fact, the AFM images of deletion mutants lacking either of the two predicted ID regions showed either the shorter or the longer tail-like structure. The macroscopic contour lengths of the shorter and longer ID regions showed wide distributions and were, on average, 17.8 and 26.2 nm, respectively. We analyzed mechanical properties (stiffness) of the observed tail-like structures by estimating the macroscopic persistence length and Young's modulus. The persistence length was approximately 11 nm for both tail-like structures. Young's modulus was approximately 9–58 MPa. This Young's modulus is two to

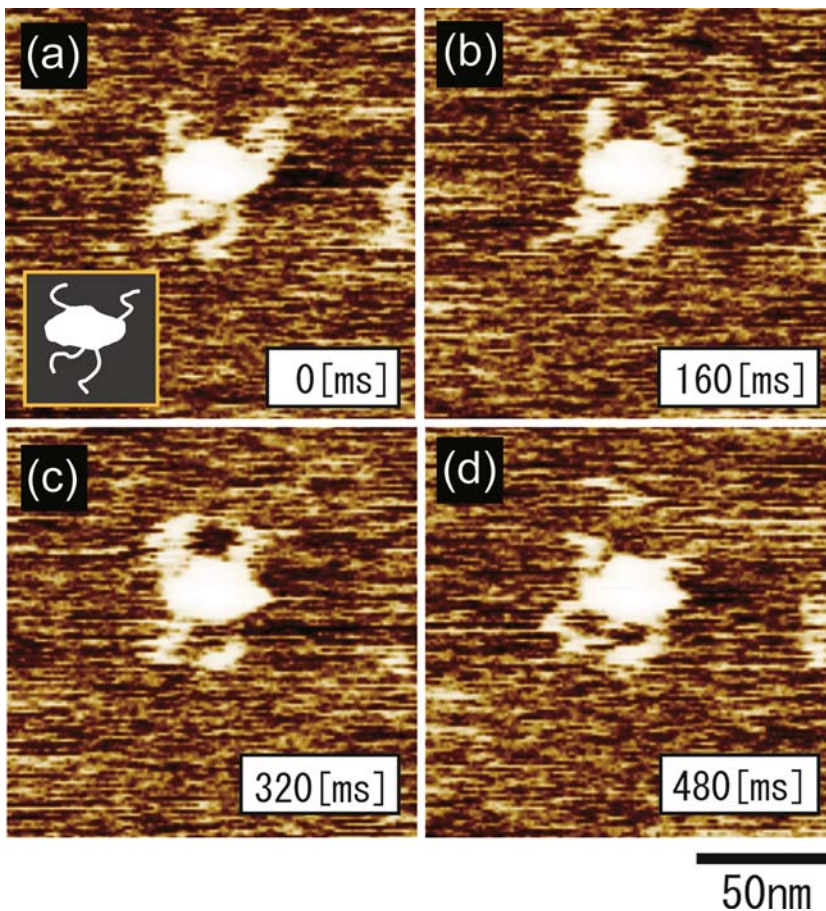


Figure 17.21. Successive atomic force microscope images of oligomerized facilitates chromatin transcription (FACT) protein captured at an imaging rate of 6 frames/sec. The scan range was 150 nm \times 150 nm. A lumpy shape and four tail-like structures can be seen (see the schematic inset in panel (a)). The position of the tail-like structures fluctuated markedly over time. The images were processed using brightness-equalizing software.

three orders of magnitude smaller than those reported for globular proteins but similar to that reported for carbonate anhydrase II incubated in the presence of 2–6 M guanidine HCl (Afrin et al., 2005), suggesting that the structures of the ID regions are similar to those of denatured proteins.

17.5.5. High-Speed Phase-Contrast Imaging

Compositional Mapping on Blended Polymers

To demonstrate that high-speed phase-contrast imaging is possible using small cantilevers and the fast phase detector described in Section 17.4.7, we first imaged poly(styrene-butadiene-styrene) (SBS) block copolymers as a test sample because SBS films are often used for phase imaging by tapping-mode AFM. Figure 17.22 shows typical (a) topographic and (b) phase images obtained simultaneously at a rate of 84 ms/frame in distilled water. Here, the phase detection timing was set at a regime in which the tip approached the surface. Clear phase-contrast images were obtained even at such a high imaging rate. In the phase-contrast images shown in Figures 17.22b, d, darker regions correspond to an advanced phase with an average shift of approximately $+6^\circ$ relative to the phase at brighter regions. Because the image contrast in the error signal is faint, the phase contrast predominantly reflects the compositional heterogeneity of the SBS film. To identify the compositions of different regions in the topographic image, the peak-to-peak set-point amplitude was reduced from 11 nm to 7 nm during imaging. Figures 17.22c, d show topographic and phase-contrast images obtained with the reduced set-point amplitude, respectively. The higher topographic region shown in Figure 17.22a was dented by the increased loading force, as shown in Figure 17.22c. The

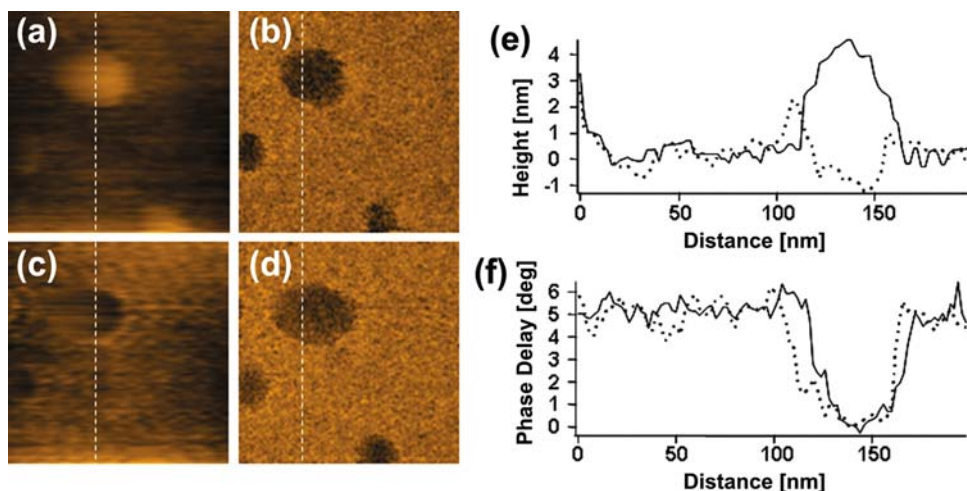


Figure 17.22. (a, c) Topographic and (b, d) phase-contrast images of a poly(styrene-butadiene-styrene) film captured at 84 ms/frame in pure water. The scan area is $200 \times 200 \text{ nm}^2$ with 100×100 pixels. (a), (b). The amplitude set-point r is 0.85, and the peak-to-peak free amplitude is 13 nm. (c), (d). The amplitude set-point is reduced to 0.54. Solid and broken lines correspond to the cross-sectional profiles (e), (f) obtained before and after reducing the amplitude set-point, respectively. Broken lines in panels a–d indicate the positions at which the cross sections were obtained.

cross-section height profiles shown in Figure 17.22e reveal that it was dented by more than 5 nm. Thus, the compositions of the higher and lower regions in Figure 17.22a are identified to be the less stiff polybutadiene (PB) and the stiff polystyrene (PS) domains, respectively. The darker (advanced phase) area in the phase-contrast image shown in Figure 17.22d is wider than that in Figure 17.22b. This is because the contact area between the tip and the surface was increased by the increased loading force. However, the magnitude of the phase shift is independent of the loading force, as can be seen in the cross-sectional phase profiles shown in Figure 17.22f. Therefore, the observed phase contrast is caused by only compositional heterogeneities and is independent of the surface topography.

We found that phase contrast largely depends on the phase-detection timing within a cantilever oscillation cycle (Uchihashi et al., 2006). A large relative phase advance was observed in the PB region when the cantilever tip approached the surface. On the other hand, only a faint phase contrast was observed when the cantilever tip was withdrawing from the surface. After analyzing this detection-timing dependence, we reached the following conclusion. A phase advance produced by energy-conservative repulsive interaction decays within one oscillating cycle due to the low Q factor of the cantilever, whereas a phase delay produced by the adhesive force does not decay quickly within a single oscillation cycle because of the energy-dissipative interaction. For more details, see the literature (Uchihashi et al., 2006; Ando et al., 2008b).

Phase-Contrast Imaging of Myosin Filaments

To demonstrate the performance of the simultaneous topographic and phase-contrast imaging of biological systems, here we show images obtained using myosin filaments in a buffer solution. Figures 17.23a, b show typical topographic and phase-contrast images, respectively, obtained at an imaging rate of 4 sec/frame. The scan area was $2\ \mu\text{m} \times 2\ \mu\text{m}$, which was relatively large for high-speed imaging, and therefore the imaging was performed at relatively slow speed. The surfaces of the myosin filaments appear smooth in the topographic image. On the other hand, the phase-contrast image shows the structures of the filaments in more detail. Here, the trigger timing was tuned so that the maximum phase contrast was

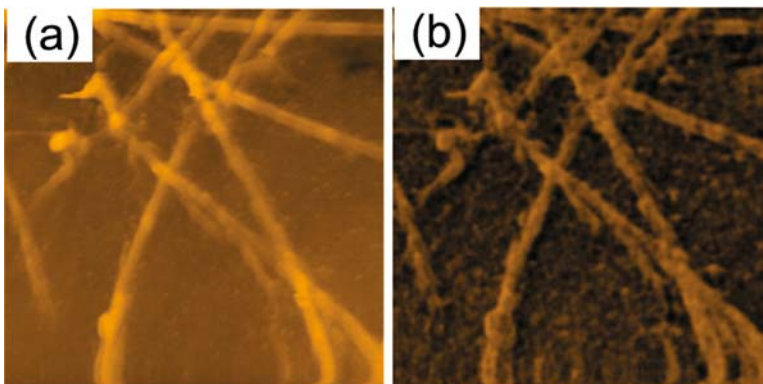


Figure 17.23. (a), (b) Topographic and phase-contrast images, respectively, of myosin filaments captured at 4 sec/frame in buffer solution. The scan area is $2 \times 2\ \mu\text{m}^2$ with 256×256 pixels.

obtained. Note that the phase on the myosin filaments is delayed relative to that on the mica surface. This is due to a large difference in the mechanical properties between the biological sample and the mica. The phase contrast on the myosin filaments indicates that the subtle variations in the mechanical properties such as elasticity and viscoelasticity exist in the myosin filaments.

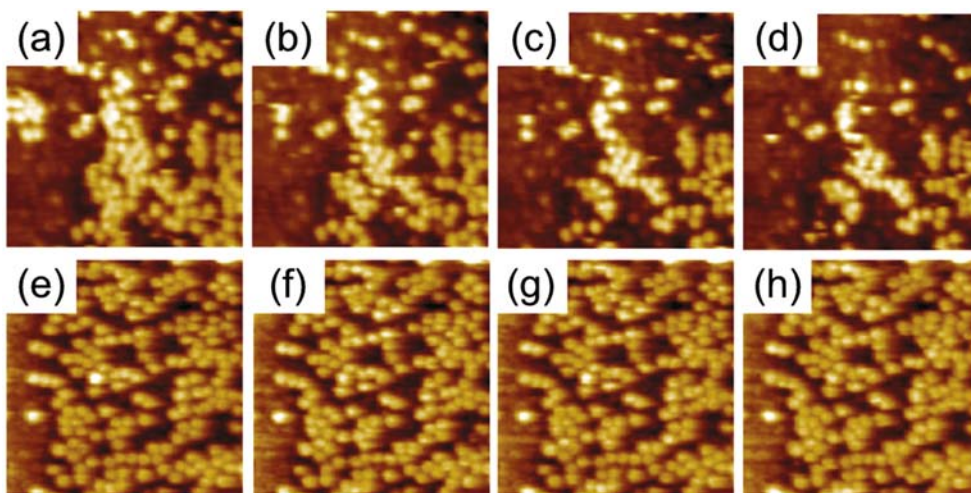


Figure 17.24. Successive atomic force microscope images of GroEL taken in (a–d) the amplitude modulation mode and (e–h) the phase modulation mode. Scan area is $400 \times 400 \text{ nm}^2$. Imaging rate is 800 ms/frame.

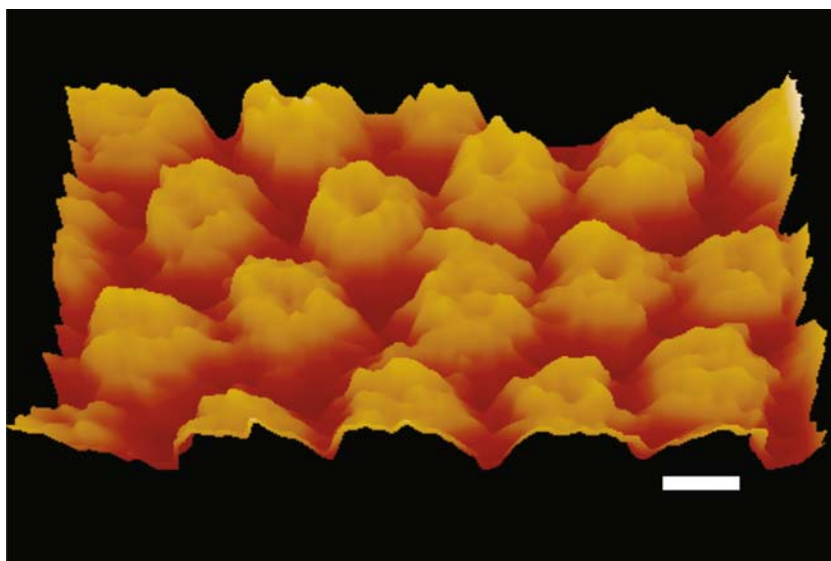


Figure 17.25. High-resolution image of GroEL taken in the phase modulation mode. Scale bar, 10 nm; imaging rate, 480 ms/frame.

Phase-Contrast Imaging of GroEL

Chaperonin GroEL was used as a test sample to show that the phase shift is more sensitive to the tip-sample interaction than the amplitude change, as its stacked ring structure is fragile and is often bisected by strong tip forces. Figures 17.24a–d show successive topographic images taken in the AM mode at 800 ms/frame. The set-point amplitude was approximately 90% of the peak-to-peak free amplitude of 7.5 nm. In these images, a large fraction of GroEL molecules are bisected and are sometimes dislodged by the scanning tip. On the other hand, in the PM mode (phase signal is used for feedback control of the tip–sample distance), the bisection of GroEL rings rarely occurred, as shown in Figures 17.24e–h. In addition, the hole centered on the ring structure is more clearly observed in the PM mode than in the AM mode, and the subunits are resolved in the PM mode (Figure 17.25).

17.6. Substrata for Observing Dynamic Biomolecular Processes

To visualize dynamic biomolecular processes, the substratum surfaces on which a sample is placed should meet various requirements; for example, (1) the surface must have an appropriate association affinity for the sample so that the sample does not move too rapidly on it, (2) the functional activity of the sample should be retained on the surface, (3) the surface should selectively attach a specific component in a multicomponent sample, and (4) the sample should attach to the surface in a desired orientation. Mica (natural muscovite or synthetic fluorophlogopite) has frequently been used as a source substratum owing to its surface flatness at the atomic level over a large area. It has net negative charge and is therefore quite hydrophilic. A bare mica surface adsorbs various proteins by electrostatic interactions. Except in some cases (such as GroEL attachment in an end-up orientation), the orientation of adsorbed proteins is not unique, and the selective attachment of a specific species is not expected. When the dynamic process of a single species of protein is to be observed without other proteins, a mica surface is useful. We can control the affinity for a specific protein by varying the ionic strength or pH or by varying the concentration of divalent cations such as Mg^{2+} . However, interesting biomolecular processes often occur in multicomponent systems.

It is desired to have, in the first step, a surface that does not initially attach to the sample. Then, this surface is modified so that only a specific species of molecules can attach to it via a linker in a desired orientation. A membrane surface with zwitterionic polar head groups such as phosphatidyl choline (PC) and phosphatidyl ethanolamine (PE) is known to resist protein adsorption (Zhang et al., 1998; Vadgama, 2005). Streptavidin is also useful for the specific attachment of a biotinylated protein because it also resists nonspecific protein adsorption. Mica-surface-supported planar lipid bilayers (Sackmann, 1996) can be easily formed from liposomes because their structure is disrupted by the strong hydrophilic interaction with the mica surface (Reviakine and Brisson, 2000). Various lipids with functional groups that are attached to polar groups [e.g., biotin attached to PE, Ni-nitrilotriacetic acid attached to phosphatidylserine] are commercially available. They enable the specific attachment of proteins labeled with biotin or his-tags onto planar lipid bilayers.

Di-oleoyl-phosphatidyl-choline (DOPC) is useful for the preparation of 2D streptavidin crystals when it is used together with biotinylated lipids (Scheuring et al., 1999; Reviakine and Brisson, 2001). It contains an unsaturated hydrocarbon in each of the two alkyl chains, which causes the bending of the chains that weakens the interaction between neighboring DOPCs. This weak interaction lowers the phase transition temperature of DOPC lipid to

about -20°C , thereby affording considerable fluidity to the planar bilayer at room temperature and thus facilitating the 2D crystal formation of streptavidin (Figure 17.26). The densely packed streptavidin does not diffuse easily. If less diffusibility is necessary, the packed streptavidin can be cross-linked using glutaraldehyde, which does not affect its ability to bind to biotin.

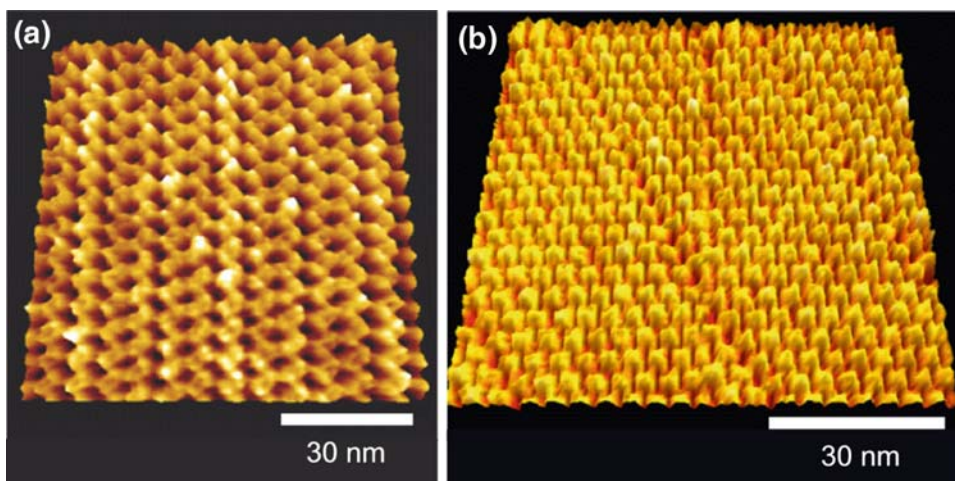


Figure 17.26. AFM images of streptavidin 2D crystals with (a) P2 (b) C222 symmetries formed at pH 5.8 and 7.4, respectively, on supported planar lipid bilayers containing biotin-lipid. The lipid compositions are DOPC, DOPS and 1,2-dioleoyl-sn-glycero-3-phosphoethanol-amine-N-(cap-biotinyl) at 7:2:1 molar ratio.

Dipalmitoyl-phosphatidyl-choline (DPPC) contains no unsaturated hydrocarbons in the alkyl chains; therefore, its phase transition temperature is high ($\sim 41^{\circ}\text{C}$), and it is suitable for preparing planar lipid bilayers with low fluidity. For example, when planar bilayers are formed using DPPC at a high temperature ($\sim 60^{\circ}\text{C}$) together with a suitable fraction of DPPE-biotin, streptavidin, which is sparsely attached to the surface, negligibly diffuses at room temperature (Ando et al., 2008a). We can anchor a biotinylated protein sparsely on this lipid bilayer surface and observe the dynamic interaction of the anchored protein with a floating counterpart protein. When the counterpart protein contains a flexible structure, it exhibits very rapid Brownian motion even when it is in contact with the anchored protein. Because such a rapidly moving structure cannot be imaged even by high-speed AFM, it is necessary to find appropriate lipid polar groups to slow the motion. In addition, the anchored protein may rapidly rotate around the biotin–streptavidin connection, which often hampers the observation of the protein–protein interaction events. To solve this problem, the protein to be anchored must be biotinylated at two appropriate sites, or the lipid polar groups should have an appropriate affinity for the anchored protein.

References

- Afrin R., M. T. Alam, and A. Ikai, Pretransition and progressive softening of bovine carbonic anhydrase II as probed by single molecule atomic force microscopy, *Protein Sci.* 14:1447–1457 (2005).
- Albrecht T. R., P. Grütter, D. Horne, and D. Rugar, Frequency modulation detection using high- Q cantilevers for enhanced force microscope sensitivity, *J. Appl. Phys.* 69:668–673 (1991).

- Anczykowski B., J. P. Cleveland, D. Krüger, V. Elings, and H. Fuchs, Analysis of the interaction mechanisms in dynamic mode SFM by means of experimental data and computer simulation, *Appl. Phys. A* 66:S885–S889 (1998).
- Ando T., N. Kodera, E. Takai, D. Maruyama, K. Saito, and A. Toda, A high-speed atomic force microscope for studying biological macromolecules, *Proc. Natl. Acad. Sci. USA* 98:12468–12472 (2001).
- Ando T., N. Kodera, D. Maruyama, E. Takai, K. Saito, and A. Toda, A high-speed atomic force microscope for studying biological macromolecules in action, *Jpn. J. Appl. Phys.* 41:4851–4856 (2002).
- Ando T., N. Kodera, Y. Naito, T. Kinoshita, K. Furuta, and Y. Y. Toyoshima, A High-speed atomic force microscope for studying biological macromolecules in action, *Chem. Phys. Chem.* 4:1196–1202 (2003).
- Ando T., T. Uchihashi, N. Kodera, A. Miyagi, R. Nakakita, H. Yamashita, and K. Matada, High-speed atomic force microscopy for capturing the dynamic behavior of protein molecules at work, *Surf. Sci. Nanotechnol.* 3:384–392 (2005).
- Ando T., T. Uchihashi, N. Kodera, A. Miyagi, R. Nakakita, H. Yamashita, and M. Sakashita, High-speed atomic force microscopy for studying the dynamic behavior of protein molecules at work, *Jpn. J. Appl. Phys.* 45:1897–1903 (2006).
- Ando T., T. Uchihashi, N. Kodera, D. Yamamoto, M. Taniguchi, A. Miyagi, and H. Yamashita, High-speed atomic force microscopy for observing dynamic biomolecular processes, *J. Mol. Recognit.* 20:448–458 (2007).
- Ando T., T. Uchihashi, N. Kodera, D. Yamamoto, A. Miyagi, M. Taniguchi, and H. Yamashita, High-speed AFM and nano-visualization of biomolecular processes, *Pflugers Arch. Eur. J. Physiol.* 456:211–225 (2008a).
- Ando T., T. Uchihashi, and T. Fukuma, High-speed atomic force microscopy for nano-visualization of dynamic biomolecular processes, *Prog. Surf. Sci.* 83:337–437 (2008b).
- Azem A., M. Kessel, and P. Goloubinoff, Characterization of a functional GroEL14(GroES7)2 chaperonin hetero-oligomer, *Science* 265:653–656 (1994).
- Bar G., Y. Thomann, R. Brandsch, H.-J. Cantow, and M.-H. Whangbo, Factors affecting the height and phase images in tapping mode atomic force microscopy. Study of phase-separated polymer blends of poly(ethene-co-styrene) and poly (2,6-dimethyl- 1,4-phenylene oxide), *Langmuir* 13:3807–3812 (1997).
- Belotserkovskaya R., S. Oh, V. A. Bondarenko, G. Orphanides, V. M. Studitsky, and D. Reinberg, FACT facilitates transcription-dependent nucleosome alteration, *Science* 301:1090–1093 (2003).
- Burgess S. A., M. L. Walker, F. Wang, J. P. Sellers, H. D. White, P. J. Knight, and J. Trinick, The prepower stroke conformation of myosin V, *J. Cell Biol.* 159:983–991 (2002).
- Burgess S. A., M. L. Walker, H. Sakakibara, P. J. Knight, and K. Oiwa, Dynein structure and power stroke, *Nature* 421:715–718 (2003).
- Burston S. G., N. A. Ranson, and A. R. Clarke, The origins and consequences of asymmetry in the chaperonin reaction cycle, *J. Mol. Biol.* 249:138–152 (1995).
- Braig K., Z. Otwinowski, R. Hegde, D. C. Boisvert, A. Joachimiak, A. L. Horwich, and P. B. Sigler, The crystal structure of the bacterial chaperonin GroEL at 2.8 Å, *Nature* 371:578–586 (1994).
- Chang W.-J., J.-C. Hsu, and T.-H. Lai, Inverse calculation of the tip-sample interaction force in atomic force microscopy by the conjugate gradient method, *J. Phys. D Appl. Phys.* 37:1123–1126 (2004).
- Cleveland J. P., B. Anczykowski, A. E. Schmid, and V. B. Elings, Energy dissipation in tapping-mode atomic force microscopy, *Appl. Phys. Lett.* 72:2613–2615 (1998).
- Czajkowsky D. M., M. J. Allen, V. Elings, and Z. Shao, Direct visualization of surface charge in aqueous solution, *Ultramicroscopy* 74:1–5 (1998).
- Darst S. A., M. Ahlers, P. H. Meller, E. W. Kubalek, R. Blankenburg, H. O. Ribi, H. Ringsdorf, and R. D. Kornberg, Two-dimensional crystals of streptavidin on biotinylated lipid layers and their interactions with biotinylated macromolecules, *Biophys. J.* 59:387–396 (1991).
- Demarest S. J., M. Martinez-Yamout, J. Chung, H. Chen, W. Xu, H. J. Dyson, R. M. Evans, and P. E. Wright, Mutual synergistic folding in recruitment of CBP/p300 by p160 nuclear receptor coactivators, *Nature* 415: 549–553 (2002).
- Forkey J. N., M. E. Quinlan, M. A. Shaw, J. E. T. Corrie, and Y. E. Goldman, Three-dimensional structural dynamics of myosin V by single-molecule fluorescence polarization, *Nature*, 422:399–404 (2003).
- Fukuma T., M. Kimura, K. Kobayashi, K. Matsushige, and H. Yamada, Development of low noise cantilever deflection sensor for multienvironment frequency-modulation atomic force microscopy, *Rev. Sci. Instrum.* 76:053704 (2005).
- Fukuma T., Y. Okazaki, N. Kodera, T. Uchihashi, and T. Ando, High resonance frequency force microscope scanner using inertia balance support, *Appl. Phys. Lett.* 92:243119 (2008).
- Gao S., L. F. Chi, S. Lenhart, B. Anczykowski, C. M. Niemeyer, M. Adler, and H. Fuchs, High quality mapping of DNA-protein complexes by dynamic scanning force microscopy, *Chem. Phys. Chem.* 6:384–388 (2001).

- Giessibl F.J., Atomic resolution of the silicon (111)-(7 × 7) surface by atomic force microscopy, *Science* 267:68–71 (1995).
- Grallert H. and J. Buchner, Review: A structural view of the GroE chaperone cycle, *J. Struct. Biol.* 135:95–103 (2001).
- Hung S. K., E.-T. Hwu, I.-S. Hwang, and L.-C. Fu, Postfitting control scheme for periodic piezoscanner driving, *Jpn. J. Appl. Phys.* 45B:1917–1921 (2006).
- Kindt J. H., G. E. Fantner, J. A. Cutroni, and P. K. Hansma, Rigid design of fast scanning probe microscopes using finite element analysis, *Ultramicroscopy* 100:259–265 (2004).
- Kitazawa M., K. Shiotani, and A. Toda, Batch fabrication of sharpened silicon nitride tips, *Jpn. J. Appl. Phys. (Pt. 1)* 42:4844–4847 (2003).
- Kodera N., H. Yamashita, and T. Ando, Active damping of the scanner for high-speed atomic force microscopy, *Rev. Sci. Instrum.* 76:053708 (2005).
- Kodera N., M. Sakashita, and T. Ando, Dynamic proportional-integral-differential controller for high-speed atomic force microscopy, *Rev. Sci. Instrum.* 77:083704 (2006).
- Kokavecz J., Z. Tóth, Z. L. Horváth, P. Heszler, and Á. Mechler, Novel amplitude and frequency demodulation algorithm for a virtual dynamic atomic force microscope, *Nanotechnology* 17:S173–S177 (2006).
- Ku A. C., S. A. Darst, C. R. Robertson, A. P. Gast, and R. D. Kornberg, Molecular analysis of two-dimensional protein crystallization, *J. Phys. Chem.* 97:3013–3016 (1993).
- Legleiter J., M. Park, B. Cusick, and T. Kowalewski, Scanning probe acceleration microscopy (SPAM) in fluids: Mapping mechanical properties of surfaces at the nanoscale, *Proc. Natl. Acad. Sci. USA* 103:4813–4818 (2006).
- Lorimer G. H., Protein folding. Folding with a two-stroke motor, *Nature* 388:720–722 (1997).
- Minezaki Y., K. Homma, A. R. Kinjo, and K. Nishikawa, Human transcription factors contain a high fraction of intrinsically disordered regions essential for transcriptional regulation, *J. Mol. Biol.* 359:1137–1149 (2006).
- Miyagi A., Y. Tsunaka, T. Uchihashi, K. Mayanagi, S. Hirose, K. Morikawa, and T. Ando, Visualization of intrinsically disordered regions of proteins by high-speed atomic force microscopy, *Chem. Phys. Chem.* 9:1859–1866 (2008).
- Reinberg D. and R. J. Sims III, de FACTo nucleosome dynamics, *J. Biol. Chem.* 281:23297–23301 (2006).
- Reviakine I. and A. Brisson, Formation of supported phospholipid bilayers from unilamellar vesicles investigated by atomic force microscopy, *Langmuir* 16:1806–1815 (2000).
- Reviakine I. and A. Brisson, Streptavidin 2D crystals on supported phospholipid bilayers: Toward constructing anchored phospholipid bilayers, *Langmuir* 17:8293–8299 (2001).
- Rye H. S., S. G. Burston, W. A. Fenton, J. M. Beechem, Z. Xu, P. B. Sigler, and A. L. Horwich, Distinct actions of cis and trans ATP within the double ring of the chaperonin GroEL, *Nature* 388:792–798 (1997).
- Rye H. S., A. M. Roseman, S. Chen, K. Furtak, W. A. Fenton, H. R. Saibil, and A. L. Horwich, GroEL–GroES cycling: ATP and nonnative polypeptide direct alternation of folding-active rings, *Cell* 97:325–338 (1999).
- Sackmann E., Supported membranes: Scientific and practical applications, *Science* 271:43–48 (1996).
- Sahin O., Harnessing bifurcations in tapping-mode atomic force microscopy to calibrate time-varying tip-sample force measurements, *Rev. Sci. Instrum.* 78:103707 (2007).
- Sahin O., S. Magonov, C. Su, C. F. Quate, and O. Solgaard, An atomic force microscope tip designed to measure time-varying nanomechanical forces, *Nat Nanotechnol.* 2:507–514 (2007).
- Sakamoto T., I. Amitani, E. Yokota, and T. Ando, Direct observation of processive movement by individual myosin V molecules, *Biochem. Biophys. Res. Commun.* 272:586–590 (2000).
- Scheuring S., D. J. Müller, P. Ringle, J. B. Heymann, and A. Engel, Imaging streptavidin 2D crystals on biotinylated lipid monolayers at high resolution with the atomic force microscope, *J. Microsc* 193:28–35 (1999).
- Schiener J., S. Witt, M. Stark, and R. Guckenberger, Stabilized atomic force microscopy imaging in liquids using second harmonic of cantilever motion for setpoint control, *Rev. Sci. Instrum.* 75:2564–2568 (2004).
- Schitter G., F. Allgöwer, and A. Stemmer, A new control strategy for high-speed atomic force microscopy, *Nanotechnology* 15:108–114 (2004).
- Shimojima T., M. Okada, T. Nakayama, H. Ueda, K. Okawa, A. Iwamatsu, H. Handa, and S. Hirose, *Drosophila* FACT contributes to Hox gene expression through physical and functional interactions with GAGA factor, *Genes Dev.* 17:1605–1616 (2003).
- Stark M. and R. Guckenberger, Fast low-cost phase detection setup for tapping-mode atomic force microscopy, *Rev. Sci. Instrum.* 70:3614–3619 (1999).
- Stark M., R. W. Stark, W. M. Heck, and R. Guckenberger, Inverting dynamic force microscopy: From signals to time-resolved interaction forces, *Proc. Natl. Acad. Sci. USA* 99:8473–8478 (2002).
- Syed S., G. E. Snyder, C. Franzini-Armstrong, P. R. Selvin, and Y. E. Goldman, Adaptability of myosin V studied by simultaneous detection of position and orientation, *EMBO J.* 25:1795–1803 (2006).

- Taguchi H., T. Ueno, H. Tadakuma, M. Yoshida, and T. Funatsu, Single-molecule observation of protein–protein interactions in the chaperonin system, *Nat Biotechnol.* 19:861–865 (2001).
- Tamayo J., and R. García, Deformation, contact time, and phase contrast in tapping mode scanning force microscopy, *Langmuir* 12:4430–4435 (1996).
- Tamayo J., A. D. L. Humphris, R. J. Owen, and M. J. Miles, High- Q dynamic force microscopy in liquid and its application to living cells, *Biophys. J.* 81:526–537 (2001).
- Uchihashi T., T. Ando, and H. Yamashita, Fast phase imaging in liquids using a rapid scan atomic force microscope, *Appl. Phys. Lett.* 89:213112 (2006).
- Vadgama P., Surface biocompatibility, *Annu. Rep. Prog. Chem. C Phys. Chem.* 101:14–52 (2005).
- Wang S.-W., C. R. Robertson, and A. P. Gast, Molecular arrangement in two-dimensional streptavidin crystals, *Langmuir* 15:1541–1548 (1999).
- Warsaw D. M., G. G. Kennedy, S. S. Work, E. B. Kremensova, S. Beck, and K. M. Trybus, Differential labeling of myosin V heads with quantum dots allows direct visualization of hand-over-hand processivity, *Biophys. J.* 88:L30–L32 (2005).
- Wulff G., Zur frage der geschwindigkeit des wachstums und der auflösung der kristallflächen *Z. Kristallogr.* 34:449–530 (1901).
- Xu Z., A. L. Horwich, and P. B. Sigler, The crystal structure of the asymmetric GroEL–GroES–(ADP)₇ chaperonin complex, *Nature* 388:741–750 (1997).
- Yamamoto D., T. Uchihashi, N. Kodera, and T. Ando, Anisotropic diffusion of point defects in two-dimensional crystal of streptavidin observed by high-speed atomic force microscopy, *Nanotechnology* 19:384009 (2008).
- Yatcilla M. T., C. R. Robertson, and A. P. Gast, Influence of pH on two-dimensional streptavidin crystals, *Langmuir* 14:497–503 (1998).
- Yifrach O. and A. L. Horovitz, Nested cooperativity in the ATPase activity of the oligomeric chaperonin GroEL, *Biochemistry* 34:5303–5308 (1995).
- Yildiz A., J. N. Forkey, S. A. McKinney, T. Ha, Y. E. Goldman, and P. R. Selvin, Myosin V walks hand-over-hand: Single fluorophore imaging with 1.5-nm localization, *Science* 300:2061–2065 (2003).
- Zhang S. F., P. Rolfe, G. Wright, W. Lian, A. J. Milling, S. Tanaka, and K. Ishihara, Physical and biological properties of compound membranes incorporating a copolymer with a phosphorylcholine head group, *Biomaterials* 19:691–700 (1998).
- Zhong Q., D. Inniss, K. Kjoller, and V. B. Elings, Fractured polymer/silica fiber surface studied by tapping mode atomic force microscopy, *Surf. Sci.* 290:L688–L692 (1993).